



AFRL-RH-FS-TR-2017-0009

**MATILDA Version-2: Rough Earth TIALD
Model for Laser Probabilistic Risk
Assessment in Hilly Terrain – Part I**

**Paul K. Kennedy
711th Human Effectiveness Wing
Airman Systems Directorate
Bioeffects Division
Optical Radiation Bioeffects Branch**

**Brian K. Flemming
Leonardo MW Ltd, 2 Crewe Road North,
Edinburgh EH5 2XS, United Kingdom**

**Daniel F. Huantes
Engility Corp**

**Matthew D. Flower
UK Ministry of Defence, MOD Abbey Wood,
Bristol BS34 8JH, United Kingdom**

March 2017

Final Report for July 2012 to March 2017

**DESTRUCTION NOTICE – Destroy by any method that will prevent disclosure of
contents or reconstruction of this document.**

**Distribution A: Approved
for public release; distribu-
tion unlimited. PA Case No:
TSRL-PA-2017-0169**

**Air Force Research Laboratory
711th Human Performance Wing
Airman Systems Directorate
Bioeffects Division
Optical Radiation Bioeffects Branch
JBSA Fort Sam Houston, Texas
78234**

NOTICE AND SIGNATURE PAGE

Using Government drawings, specifications, or other data included in this document for any purpose other than Government procurement does not in any way obligate the U.S. Government. The fact that the Government formulated or supplied the drawings, specifications, or other data does not license the holder or any other person or corporation; or convey any rights or permission to manufacture, use, or sell any patented invention that may relate to them.

This report was cleared for public release by the 88th ABW Public Affairs Office and is available to the general public, including foreign nationals. Copies may be obtained from the Defense Technical Information Center (DTIC) (<http://www.dtic.mil>).

MATILDA Version-2: Rough Earth TIALD Model for Laser Probabilistic Risk Assessment in Hilly Terrain – Part I

(AFRL-RH-FS-TR- 2017 - 0009) has been reviewed and is approved for publication in accordance with assigned distribution statement.

KENNEDY.PAUL.K.1231446318

Digitally signed by
KENNEDY.PAUL.K.1231446318
DN: c=US, o=U.S. Government, ou=DoD,
ou=PKI, ou=USAF,
cn=KENNEDY.PAUL.K.1231446318
Date: 2017.03.15 14:01:29 -05'00'

Paul Kennedy
Work Unit Manager
Optical Radiation Bioeffects Branch

AUTREY.JEFFREY.J.1241299976

Digitally signed by AUTREY.JEFFREY.J.1241299976
DN: c=US, o=U.S. Government, ou=DoD, ou=PKI,
ou=USAF, cn=AUTREY.JEFFREY.J.1241299976
Date: 2017.05.11 15:12:44 -05'00'

JEFFREY J. AUTREY, Lt Col, USAF, BSC
Acting Chief, Bioeffects Division
Airman Systems Directorate
711th Human Performance Wing
Air Force Research Laboratory

This report is published in the interest of scientific and technical information exchange, and its publication does not constitute the Government's approval or disapproval of its ideas or findings.

REPORT DOCUMENTATION PAGE				Form Approved OMB No. 0704-0188	
Public reporting burden for this collection of information is estimated to average 1 hour per response, including the time for reviewing instructions, searching existing data sources, gathering and maintaining the data needed, and completing and reviewing this collection of information. Send comments regarding this burden estimate or any other aspect of this collection of information, including suggestions for reducing this burden to Department of Defense, Washington Headquarters Services, Directorate for Information Operations and Reports (0704-0188), 1215 Jefferson Davis Highway, Suite 1204, Arlington, VA 22202-4302. Respondents should be aware that notwithstanding any other provision of law, no person shall be subject to any penalty for failing to comply with a collection of information if it does not display a currently valid OMB control number. PLEASE DO NOT RETURN YOUR FORM TO THE ABOVE ADDRESS.					
1. REPORT DATE (DD-MM-YYYY) 13-03-2017		2. REPORT TYPE FINAL Technical Report		3. DATES COVERED (From - To) July 2012 to March 2017	
4. TITLE AND SUBTITLE MATILDA Version-2: Rough Earth TIALD Model for Laser Probabilistic Risk Assessment in Hilly Terrain – Part I				5a. CONTRACT NUMBER FA8650-14-D-6519	
				5b. GRANT NUMBER	
				5c. PROGRAM ELEMENT NUMBER	
				5d. PROJECT NUMBER	
6. AUTHOR(S) Paul K. Kennedy, Brian K. Flemming, Daniel F. Huantes, Matthew D. Flower				5e. TASK NUMBER	
				5f. WORK UNIT NUMBER H07T	
				8. PERFORMING ORGANIZATION REPORT	
7. PERFORMING ORGANIZATION NAME(S) AND ADDRESS(ES) Air Force Research Laboratory 711th Human Performance Wing Airman Systems Directorate Bioeffects Division Optical Radiation Bioeffects Branch JBSA, Fort Sam Houston, Texas 78234				8. PERFORMING ORGANIZATION REPORT	
9. SPONSORING / MONITORING AGENCY NAME(S) AND ADDRESS(ES) 711th Human Effectiveness Wing Airman Systems Directorate Bioeffects Division Optical Radiation Bioeffects Branch JBSA, Fort Sam Houston, Texas 78234				10. SPONSOR/MONITOR'S ACRONYM(S) 711 HPW/RHDO	
				11. SPONSOR/MONITOR'S REPORT NUMBER(S) AFRL-RH-FS-TR-2017-0009	
12. DISTRIBUTION / AVAILABILITY STATEMENT Distribution A: Approved for public release; distribution unlimited. PA Case No: TSRL-PA-2017-0169					
13. SUPPLEMENTARY NOTES					
14. ABSTRACT Over the past 15 years, the United Kingdom (UK) Ministry of Defence (MoD) and the United States (US) Air Force Research Laboratory (AFRL) have collaborated to develop a US-UK laser range safety tool, the Military Advanced Technology Integrated Laser hazard Assessment (MATILDA) tool. MATILDA uses Probabilistic Risk Assessment (PRA) techniques to perform laser safety and hazard analysis in support of airborne laser designator use during test and training exercises on military ranges. The initial MATILDA tool, MATILDA PRO Version-1.6.1, was based on the 2007 PRA model developed to perform range safety clearances for the UK Thermal Imaging Airborne Laser Designator (TIALD) system. The 2007 TIALD model was an approximation that assumed flat terrain on the range (Smooth Earth TIALD Model), a conservative approximation valid in all terrain. Over the past five years, however, an enhanced version, MATILDA PRO Version-2.0.3, has been produced. The enhanced tool is based on an updated (2012) TIALD model, which has more complex PRA algorithms appropriate for hilly terrain (Rough Earth TIALD Model). For reasons of length, documentation of the mathematical algorithms and computational procedures incorporated in MATILDA PRO Version-2.0.3 has been divided between two AFRL Technical Reports. This Technical Report, designated Part I, contains documentation of the computational procedures for probabilistic fault/failure laser hazard analysis. The second Technical Report, designated Part II, will document the fault-free laser hazard analysis.					
15. SUBJECT TERMS					
16. SECURITY CLASSIFICATION OF: Unclassified			17. LIMITATION OF ABSTRACT ii U	18. NUMBER OF PAGES 68	19a. NAME OF RESPONSIBLE PERSON Paul Kennedy
a. REPORT U	b. ABSTRACT U	c. THIS PAGE U			19b. TELEPHONE NUMBER (include area code) NA

Distribution A: Approved for public release; distribution unlimited. PA Case No: TSRL-PA-2017-0169

Standard Form 298 (Rev. 8-98)

Prescribed by ANSI Std. Z39.18

The opinions expressed on this document, electronic or otherwise, are solely those of the author(s). They do not represent an endorsement by or the views of the United States Air Force, the Department of Defense, or the United States Government.

This Page Intentionally Left Blank

TABLE OF CONTENTS

TABLE OF CONTENTS.....	v
LIST OF FIGURES	vii
LIST OF TABLES	viii
ACRONYMS.....	ix
ABSTRACT.....	1
1 INTRODUCTION.....	1
2 UK LASER PRA MODEL AND MATILDA COMPUTATIONAL MODELS.....	3
2.1 UK Laser PRA Model.....	3
2.2 MATILDA Version-1.6.1 and the Smooth Earth TIALD Model	8
2.3 MATILDA Version-2.0.3 and the Rough Earth TIALD Model	12
3 CALCFAULT: REVISED GROUND PLANE COMPUTATION.....	13
3.1 CALCFAULT Computation in the Ground Plane	13
3.2 Single Pulse Expectation Value: Ground Plane Computation	15
3.3 Display Plane Coordinate Systems for Laser Pointing Errors	16
3.4 Colatitude and Longitudinal Angles	19
3.5 Laser Pointing Error Distribution Function in the Display Plane	24
3.6 Jacobian Function in Orthogonal Coordinates	28
3.7 Single Pulse Expectation Value: Numerical Evaluation	36
4 3D-CALCFAULT: DISPLAY PLANE COMPUTATION	40
4.1 CALCFAULT Computation in the Display Plane	40
4.2 Single Pulse Expectation Value: Display Plane Computation	41
4.3 Evaluation of Elemental Spherical Surface Area	42
4.4 Single Pulse Expectation Value: Numerical Evaluation	47
4.5 Comparison of Ground Plane and Display Plane Methods.....	50
5 CONCLUSIONS	60
6 REFERENCES	63

LIST OF FIGURES

Figure 1: The “PE-PI-POD” Catastrophic Chain of Events Model.....	6
Figure 2: Fault-Free Overshoot & Undershoot.....	10
Figure 3: Laser Pointing Error Coordinate Systems.....	17
Figure 4: Aircraft - Target Geometry.....	20
Figure 5: Aircraft Display Axes.....	21
Figure 6: Colatitude and Longitude.....	22
Figure 7: Longitude.....	23
Figure 8: Spherical Coordinate System.....	25
Figure 9: Probability of a Laser Pointing Error.....	26
Figure 10: Laser Projection Geometry.....	29
Figure 11: Aircraft Path Geometry.....	29
Figure 12: Aircraft Positions in Four Quadrants.....	31
Figure 13: Pointing Error Cone Projection.....	33
Figure 14: Orthogonal Pointing Error Cone Projection.....	33
Figure 15: Volume in a Bivariate Integral.....	39
Figure 16: Display Axes Coordinate Systems.....	44
Figure 17: Spherically Projected Array of Ground Points.....	45
Figure 18: Spherical Triangle.....	46
Figure 19: Aircraft Display Axes: Aircraft Aligned with MICS Axes.....	52
Figure 20: Aircraft Display Axes: Aircraft Located in MICS Quadrants.....	53
Figure 21: Attack Track Expectation Value: 500 m and 250 m Resolution.....	58
Figure 22: Attack Track Expectation Value: 100 m and 25 m Resolution.....	59

LIST OF TABLES

Table 1: Laser System Parameters for the Test Case Airborne Laser Designator.....	54
---	----

ACRONYMS

UK/MoD	United Kingdom Ministry of Defence
US/AFRL	United States Air Force Research Laboratory
MATILDA	Military Advanced Technology Integrated Laser hazard Assessment
PRA	Probabilistic Risk Assessment
TIALD	Thermal Imaging Airborne Laser Designator
DoD	Department of Defense
HEL	High Energy Laser
MPE	Maximum Permissible Exposure
PA	Project Arrangement
CRA	Controlled Range Area
GUI	Graphic User Interface
GIS	Geographic Information System
DTED	Digital Terrain Elevation Data
NASA	National Aeronautics and Space Administration
NOHD	Nominal Ocular Hazard Distance
ALARP	As Low As Reasonably Practicable
MOVL	Minimum Ophthalmoscopically Visible Lesion
LSP	Laser Safety Paper
PCRM	Probabilistic Range Clearance Model
PDF	Probability Distribution Function
MSD	Minimum Separation Distance
FFLFZ	Fault-Free Laser Firing Zone
MKS	Meters, Kilograms, Seconds
MICS	MATILDA Internal Coordinate System
CALF	Circle of Allowed Laser Firing
LOS	Line of Sight
PDE	Probability Density Element

ABSTRACT

Over the past 15 years, the United Kingdom (UK) Ministry of Defence (MoD) and the United States (US) Air Force Research Laboratory (AFRL) have collaborated to develop a US-UK laser range safety tool, the Military Advanced Technology Integrated Laser hazard Assessment (MATILDA) tool. MATILDA uses Probabilistic Risk Assessment (PRA) techniques to perform laser safety and hazard analysis in support of airborne laser designator use during test and training exercises on military ranges. The initial MATILDA tool, MATILDA PRO Version-1.6.1, was based on the 2007 PRA model developed to perform range safety clearances for the UK Thermal Imaging Airborne Laser Designator (TIALD) system. The 2007 TIALD model was an approximation that assumed flat terrain on the range (Smooth Earth TIALD Model), a conservative approximation valid in all terrain. Over the past five years, however, an enhanced version, MATILDA PRO Version-2.0.3, has been produced. The enhanced tool is based on an updated (2012) TIALD model, which has more complex PRA algorithms appropriate for hilly terrain (Rough Earth TIALD Model). For reasons of length, documentation of the mathematical algorithms and computational procedures incorporated in MATILDA PRO Version-2.0.3 has been divided between two AFRL Technical Reports. This Technical Report, designated Part I, contains documentation of the computational procedures for probabilistic fault/failure laser hazard analysis. The second Technical Report, designated Part II, will document the fault-free laser hazard analysis.

1 INTRODUCTION

Over the past 20 years, the US Department of Defense (DoD) has funded the development of airborne, ground-based, and ship-borne High Energy Laser (HEL) weapons systems, primarily for Counter-Rocket, Artillery, and Mortar applications. The development, and potential deployment, of an increasingly wide range of military laser systems with higher energies, and hence, greater hazard potential, is leading to a requirement for more sophisticated means of assessing the real risk of hazardous exposure to operational personnel and strategic assets. Standard deterministic risk analysis methods [1,2], based on Maximum Permissible Exposure (MPE) limits [3,4], are inadequate to assess the potential risk posed by test and deployment of HEL systems. Deterministic models do not account for the unpredictable errors that inevitably occur in outdoor range tests, training, and/or operational use. They also give only a binary safe/unsafe assessment, without providing a quantitative risk assessment for “unsafe” scenarios.

Recently, attention in the DoD has turned to Probabilistic Risk Assessment (PRA) models [5,6] as an alternative for performing laser hazard analysis for high output lasers in outdoor environments [7-12]. These models can incorporate errors and uncertainties, using probability distribution functions, and they can provide a quantitative probability of injury to personnel or damage to hardware. Over the past 15 years, in response to DoD requirements, the United States (US) Air Force Research Laboratory (AFRL) has collaborated with the United Kingdom (UK) Ministry of Defence (MoD) to develop a jointly-owned, PRA-based, laser range safety tool, the Military Advanced Technology Integrated Laser hazard Assessment (MATILDA) tool [13-17]. This collaboration has been covered, sequentially, by two US-UK Project Arrangements (PAs): No. DOD-MOD-AF-06-0004 (2007-2012) and No. DOD-MOD-AF-12-0004 (2012-2017).

The UK MoD has been using laser PRA models to support military laser tests at UK ranges for the past 40 years. PRA analysis is essential for range testing in the UK, where ranges are typically quite small and located near to populated areas. Only by quantifying laser hazards using PRA, and comparing these to a maximum acceptable risk level, can the MoD authorize laser testing on small ranges, where the beam has a finite probability of escaping the Controlled Range Area (CRA). The US-UK collaboration was initiated because the USAF considered it highly desirable to leverage UK expertise in this area, with the long term goal of producing probabilistic laser safety tools to meet future DoD laser safety needs. The quid pro quo was a trade of UK expertise in probabilistic laser hazard analysis and PRA mathematical modeling for US expertise in the development of advanced software tools for laser hazard analysis and laser range safety.

Initial MATILDA code development (2007–2012) was based on the PRA “partition” model developed to perform range safety clearances for the UK Thermal Imaging Airborne Laser Designator (TIALD) system. The TIALD model “fault-free” laser hazard analysis is geometrically similar to the standard risk analysis methods currently used for laser safety clearances on US ranges [1]. However, the TIALD model contains an additional probabilistic hazard analysis component, which assesses probability of injury to an unprotected person outside of the CRA in the event of a fault or failure in the laser directional control system. The TIALD model was chosen as the basis for the initial MATILDA tool because it was the most advanced UK laser PRA model available at the time when code development began (2007).

The final deliverable (2012) under the first PA was a code designated MATILDA PRO Version-1.6.1, which was a tested and validated software tool containing the complete 2007 TIALD model. It included a calculation of safe firing zones for fault-free operation, calculation of the probability of injury to an observer off the range in the event of system fault/failure, and a sophisticated graphics and terrain mapping package to illustrate the results. The Graphic User Interface (GUI) was based on open-source Geographic Information System (GIS) technology that integrates relevant laser system performance parameters with environmental data appropriate to the range location where the system is being operated. A previous AFRL Technical Report [16] documented the mathematical algorithms and computational procedures incorporated in MATILDA PRO Version-1.6.1, and provided the mathematical basis for future code development and improvements.

Advanced MATILDA code development (2012-2017), under the second PA, has been based on incorporation of an updated TIALD model. The 2007 TIALD model was an approximation that assumed flat terrain on the range (Smooth Earth Model). The Smooth Earth Model is a conservative approximation in laser safety terms, since hills and elevated terrain generally provide shielding and reduce risk. A less conservative and more realistic model was desirable, however, since it would produce reduced hazard estimates and fewer constraints on range tests. By 2012 an updated TIALD model had been developed, with more complex PRA algorithms appropriate for hilly terrain (Rough Earth TIALD Model). This model uses input data from the Digital Terrain Elevation Data (DTED) database, developed by the National Aeronautics and Space Administration (NASA). The final deliverable under the second PA will be a code designated MATILDA PRO Version-2.0.3, which is a tested and validated software tool containing the complete Rough Earth TIALD Model.

For reasons of length, documentation of the mathematical algorithms and computational procedures incorporated in MATILDA PRO Version-2.0.3 has been divided between two AFRL

Technical Reports, which will once again provide the mathematical basis for future code development. This Technical Report, designated Part I, contains documentation of the computational procedures for probabilistic fault/failure laser hazard analysis. The second Technical Report, designated Part II, will document the fault-free laser hazard analysis. Section 2 of this report gives a brief summary and overview of the UK Laser PRA Model, the Smooth Earth TIALD Model, and the computational structure of the Rough Earth TIALD Model. Section 3 documents the revisions that have been made since 2012 in the old CALCFAULT module, which performs the probabilistic fault/failure hazard evaluation in the Ground Plane of the target, using Cartesian Coordinates. The revisions were necessary to provide continuity with the new 3D-CALCFAULT module, documented in Section 4, which performs the probabilistic fault/failure hazard evaluation in the Display Plane of the aircraft, using Spherical Coordinates. Section 4 also contains a comparison of the ground plane and display plane evaluation methods. Sections 5 and 6 give conclusions and references.

2 UK LASER PRA MODEL AND MATILDA COMPUTATIONAL MODELS

The UK Laser PRA Model and the risk-based approach to laser hazard assessment that underlies it has already been extensively documented in past open source publications [11-17], and technical approach and solution reporting can be found in depth within the initial AFRL Technical Report [16], which documented MATILDA PRO Version-1.6.1 and its' Computational Model (Smooth Earth TIALD Model). Only a brief overview and summary of the UK Laser PRA Model and the Smooth Earth TIALD Model is given in Sections 2.1 and 2.2 of this report, with the reader directed to past work for a more extensive and detailed description. Section 2.3 gives a brief overview of the Computational Model underlying MATILDA PRO Version-2.0.3 (Rough Earth TIALD Model), with an eye to setting the stage for the detailed documentation of this model given in later Sections.

2.1 UK Laser PRA Model

The primary hazard associated with the use of low-to-moderate power lasers on military ranges is potential injury to exposed tissue, in particular the eye. While protective measures can be applied for persons within the CRA, the main concern – particularly in the case of airborne laser target designators and rangefinders – is avoidance of possible ocular injury to unprotected members of the general public, should laser energy escape the confines of the range. The goal of the UK Laser PRA Model is to quantify the expectation value of ocular damage to unprotected observers outside the CRA, based on range geometry, target location on the range, location and population density of surrounding urban areas, laser system parameters (including laser pointing errors during no-fault operation and fault conditions), and the planned laser firing locations during the test or training scenario. For airborne laser-target designators, which have been the primary focus of UK PRA hazard analysis, the flight height and attack track of the aircraft carrying the laser designator defines possible firing locations [16].

Traditionally, the ocular hazards associated with a laser's output have been assessed in terms of the MPE, from which a corresponding Nominal Ocular Hazard Distance (NOHD) is determined [3,4]. The NOHD represents a safe viewing distance, and the area or volume inside the NOHD is a hazard zone, within which an unprotected observer is at risk of ocular injury. Where sufficient real estate is available, it is possible to ensure confinement of the hazard zone within the CRA, without imposing onerous restrictions on the permitted laser firing envelope. In such cases, the laser energy is said to have been "back-stopped" within the range. Should laser energy escape the CRA, however, it is possible that an unprotected observer could have an ocular injury. In such cases the zero risk criterion, implicit in standard deterministic risk analysis, creates a significant problem for those generating range safety clearances for laser testing and training.

The UK Laser PRA Model acknowledges that there is always a finite risk of laser energy escaping the CRA, especially during laser fault conditions, and that the actual risk of injury is always non-zero, although it may be negligible. The relatively small size of UK ranges enhances this risk. Thus, the stringent limitations on laser firing, required to satisfy a zero risk criterion, make standard MPE-based risk analysis too inflexible for UK range clearance requirements. Instead, UK range clearance models are probabilistic, and based on the principle of residual risk being "As Low As Reasonably Practicable" (ALARP) [2]. The use of the ALARP principle in UK hazard assessment arises from the provisions of the UK *Health and Safety at Work Act* of 1974 [18]. Given non-zero risks, use of the NOHD as a criterion for risk analysis is unsatisfactory, since it does not *quantify* the probable risk of injury for unprotected observers inside the hazard zone. The UK Laser PRA Model thus uses a probabilistic ocular damage model for 1064 nm laser energy, a "dose-response" model, to assess probability of injury. The model is based on laser biological injury data, and relates the dose and the total intra-ocular energy to the response, for determining the probability of causing a Minimum Ophthalmoscopically Visible Lesion (MOVL) [7].

ALARP requirements can only be satisfied by the use of a risk-based approach to laser hazard assessment. The outcome of such a risk-based approach is a risk management process, by which adverse events, and the inherent uncertainties with which they occur, can be rigorously identified and mitigated. The UK risk assessment process comprises two distinct stages. The *risk analysis stage* constitutes a hazard assessment of the laser system *performance* when operating either as intended, or in the event of a laser sightline directional control system fault or failure. The laser system hazard assessment in the UK is expressed formally in a Laser Safety Paper (LSP). The hazard assessment for the laser system *operation* is the subject of the *risk management and control stage*. The Probabilistic Range Clearance Model (PRCM) provides a means by which hazards arising from the laser system *operation* can be evaluated, and is based on the performance assessment described in the LSP. Laser firing restrictions for a given range, target and attack profile combination are generated by application of the PRCM, as encoded in the MATILDA tool.

The risk of an adverse event, such as a laser-induced ocular injury in an unprotected population, can be expressed in terms of a "risk chain" comprising three main components [19]: (i) a risk source, (ii) an exposure process and (iii) a causal process. This is illustrated in Figure 1. Uncertainty persists within both the exposure and causal processes over the occurrence of given events, such as the misdirection of laser energy in a specific direction or the sustaining of an ocular injury. The likeliness of an event occurring may be defined by a fixed value, for simple models, or

by a Probability Distribution Function (PDF) for more complex ones. The General Risk Model thus falls naturally into a probabilistic structure, the “ P_E - P_I - P_{OD} ” catastrophic chain of events structure, also shown in Fig. 1. The PCRM, mentioned previously, is the mathematical implementation of the “ P_E - P_I - P_{OD} ” chain of adverse risk events model. Here the “ P_E - P_I ” couplet represents the exposure process and the “ P_{OD} ” element represents the causal process. The “ P_E - P_I - P_{OD} ” structure provides the mathematical basis for the UK probabilistic laser hazard assessment.

As a start to constructing a mathematical model of the probabilistic laser hazard assessment, the risk chain must be broken down into its individual probabilistic elements. The three main components of such a risk chain are: (i) the probability of laser energy being fired in an inappropriate direction outside the Controlled Range Area (P_E), (ii) the probability of an unprotected observer being irradiated by the laser energy (P_I), and (iii) the subsequent probability of the irradiated observer sustaining an ocular injury (P_{OD}). These three components can be further decomposed into five distinct elements: i) the risk of laser energy being directed outside the CRA; ii) the risk of an unprotected observer being irradiated; iii) the risk of the unprotected observer looking in the direction of the laser energy (ocular irradiation); iv) the risk of atmospheric scintillation increasing the radiant exposure entering the eye; and v) the risk of the received radiant exposure causing ocular damage. Here, the first element is associated with P_E , the second and third with P_I , and the fourth and fifth with P_{OD} .

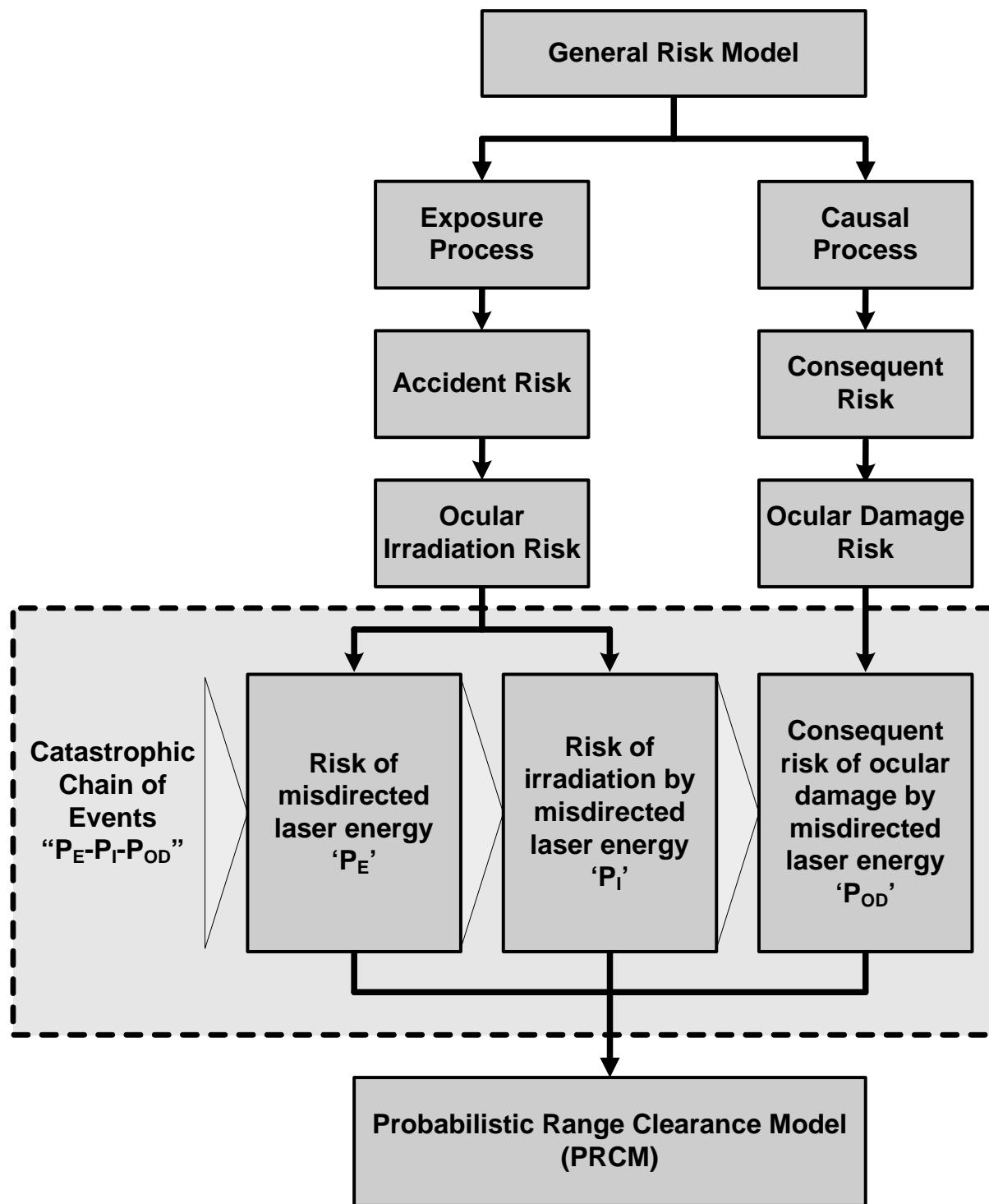


Figure 1: The “ P_E - P_I - P_{OD} ” Catastrophic Chain of Events Model

UK risk-based range clearance models have been based primarily on two of the three components: a probabilistic laser pointing error model (P_E), coupled with a probabilistic ocular damage

model for 1064 nm laser energy (P_{OD}). These have been described in detail in previous documentation [16]. In contrast, due to the complexity of accurately determining the probability of an observer being at a particular location, or looking into the laser beam, the P_I component has usually been implemented in a highly simplified version; i.e., these probabilities are typically set to unity. The inherent pessimism of this approach can then be mitigated by estimating the *expected number* of observers sustaining a given level of ocular damage in any given laser firing direction, based on the size of the beam footprint and the local population density. For this reason the UK probabilistic hazard assessment model is also referred to as the UK Expectation Model.

As indicated above, the UK Expectation Model, which incorporates the P_E - P_I - P_{OD} structure, is based on an evaluation of the expected number of unprotected observers who sustain a MOVL during an airborne laser firing maneuver, a quantity defined as E_{MOVL} . The Primary Criterion for clearance of a laser firing maneuver is that the expected number of cases of MOVL does not exceed a pre-defined maximum acceptable value, $E_{MOVLMAX}$. A typical maximum acceptable expectation value for UK range clearances is 10^{-8} occurrences of MOVL per attack. (In comparison, a typical NASA acceptable expectation value, for injury by falling inert debris, is 10^{-6} injuries per launch.) If the Primary Criterion is exceeded, then restrictions on the laser firing envelope are imposed to reduce risk to acceptable levels. Note that the very low risk levels set by the Primary Criterion are principally achieved by ensuring that most of the laser energy falls within the CRA.

Once the Primary Criterion is met then two additional precautions, the Secondary and Tertiary Precautions, are applied to identify any additional restrictions on the laser firing envelope. The Secondary and Tertiary Precautions guard against the possibility of a low likelihood, high impact event, in which a high probability of ocular damage to an irradiated observer could be masked by a low frequency of occurrence. The Secondary Precaution evaluates the expected hazard for a scenario in which it is assumed that laser energy is misdirected towards a populated area outside the CRA. The acceptable criterion for the Secondary Precaution is that – should laser energy be inadvertently misdirected outside the CRA – the expected number of cases of MOVL does not exceed a maximum *conditional* expectation value, E_{CONMAX} . For the UK, a typical maximum value for the Secondary Precaution is on the order of 10^{-3} to 10^{-4} occurrences of MOVL per attack.

The Tertiary Precaution assumes that an unprotected observer has actually been irradiated by a single pulse of laser energy. The acceptable criterion for the Tertiary Precaution is that the probability of a MOVL for an irradiated individual does not exceed a pre-defined maximum value, $P_{MOVLMAX}$. For the UK, a typical maximum value for the Tertiary Precaution is 10^{-1} occurrences of MOVL per attack. The effect of the Tertiary Precaution is to impose a probabilistically defined Minimum Separation Distance (MSD) between the laser and any unprotected observer outside the CRA. In summary, appropriate restrictions are imposed on the laser firing envelope to ensure that the Primary Criterion, Secondary Precaution, and Tertiary Precaution, are satisfied.

The final topic dealt with in this brief overview of the UK Laser PRA Model is the UK Partition Model, which determines both the computational structure of the UK TIALD model and its implementation in the MATILDA tool. The UK Partition Model is a specific implementation of the UK Expectation Model described above, in which the hazard contributions arising from fault-free and fault/failure operation of the laser directional control system are “partitioned” and evaluated separately. The overall clearance restrictions defining the permitted laser firing envelope

are a composite of the separately and sequentially evaluated restrictions for fault-free and fault/failure operation.

The fault-free portion of the Partition Model is fundamentally a geometric implementation of the hazard analysis, based on where in the terrain laser pulses are expected to fall. Laser pulses emitted during fault-free laser operation, which will be the majority of pulses fired during most attack runs, will be constrained to fall within the CRA by geometric restrictions on aircraft operations generated during the fault-free analysis. Consequently, any hazard to the population surrounding the range will come from the relatively small number of pulses, which could be emitted during fault/failure operation and which might fall outside the CRA. The hazard from these pulses is determined by a full probabilistic hazard analysis incorporating the PE-Pi-POD structure described above.

The primary products of the fault-free laser hazard analysis are the Fault-Free Laser Firing Zones for aircraft flying at each altitude of interest. A Fault-Free Laser Firing Zone (FFLFZ) is a geometric area within which an aircraft flying at a designated altitude can fire freely at the target. For any given attack altitude, the FFLFZ is defined in such a way that all fault-free laser pointing errors, which are less than or equal to the maximum fault-free pointing error, produce laser beams that fall within the CRA. Typically, the FFLFZ are evaluated for all compass directions around the target, and over a range of aircraft altitudes, in accordance with laser system user requirements. Each designated aircraft altitude produces a different FFLFZ. The geometry of the FFLFZ calculation is similar to the standard risk analysis methods currently used by the USAF to establish a safe laser firing envelope [1]. However, the FFLFZ calculation is designed to maximise the range-to-target at which the laser can be fired, given the extent of CRA available.

The hazard analysis for fault/failure operation is the fully probabilistic portion of the overall laser hazard assessment. It follows computation of the FFLFZ, considers laser pointing errors in excess of the maximum fault-free pointing error and is only performed for specific laser firing maneuvers on specific aircraft attack tracks. Thus, the first step in the fault hazard analysis is to define the aircraft attack track, attack altitude, and laser firing positions. A check is then made to ensure that the attack scenario complies with FFLFZ restrictions. Any laser firing maneuvers which do not comply with FFLFZ restrictions are eliminated prior to the fault hazard analysis. Next, the probabilistic Expectation Model is used to evaluate E_{MOVL} , and this is compared to the maximum acceptable value, $E_{MOVLMAX}$, to determine whether the specified laser firing maneuver meets the Primary Criterion for safety clearance. Finally, if the Primary Criterion is met, then the Secondary and Tertiary Precautions are applied, to identify any additional restrictions on the laser firing envelope.

2.2 MATILDA Version-1.6.1 and the Smooth Earth TIALD Model

In MATILDA Version-1.6.1, the Partition/Expectation Model is implemented by means of a Computational Model known as the Smooth Earth TIALD Model, from which the applicable laser firing restrictions are derived. The Smooth Earth TIALD Model is composed of three main modules, executed sequentially, called RBPROG, CALCZONE, and CALCFAULT. Prior to execution of these modules the input data required for the hazard assessment are first specified. There are five types of input data required for a full MATILDA analysis: i) population data for the urban and rural areas surrounding the range; ii) laser system parameters; iii) aircraft attack

track data; iv) terrain mapping and terrain elevation data; and v) geometric and geographic data defining the range and areas surrounding it. The latter includes range boundaries, target position on the range, location and boundaries of Urban Areas, and natural geographic features such as rivers, lakes, and coastlines.

The MATILDA tool is currently designed for PRA analysis of air-to-ground laser-target engagements, with an airborne laser designator that is a multiple pulse “all-round line-of-sight” system mounted on a strike aircraft. Important MATILDA input parameters for the laser system include: i) pulse energy, peak irradiance, and beam energy distribution; ii) other key beam parameters such as wavelength, beam divergence, pulse duration, and pulse repetition frequency; iii) Fault-Free and Fault Pointing Error Distributions; and iv) the Probability of Fault for the laser system. These laser system parameters are obtained by the laser system manufacturer, through testing of multiple laser units and averaging of performance data. The data is provided to laser safety officers in the Laser Safety Paper.

The five data types described above may initially be available to the analyst in a variety of physical units. For consistency a single system of units must be used in computations. The Meters, Kilograms, Seconds (MKS) unit system has been chosen for MATILDA and, with some specific exceptions, all data not initially available in MKS units are transformed into them prior to input. Another potential problem is that some geographic data types may initially be available in a variety of coordinate systems, typically local (grid-based) map coordinate systems. For computational consistency these are transformed into a single common coordinate system, termed the MATILDA Internal Coordinate System (MICS). In order to bring such local map data into the MICS, three different coordinate transformations are performed. These coordinate transformations have been described in earlier documentation [16] and will not be discussed here.

After data input and data transformations are complete, there is one additional set-up procedure which must be performed prior to initiating the computational analysis: generation of a mathematical model termed the Terrain Profile Surface, using the digital terrain elevation data and target location supplied. Although the Smooth Earth TIALD Model assumes a flat range, a conservative safety analysis requires that *some* allowance must be made for terrain elevation in the area surrounding the target, if only to guard against the possibility of short-range irradiation of elevated terrain areas where unprotected persons might be present. The Terrain Profile Surface is a simplified representation of the terrain elevation in the area surrounding the target. This theoretical surface has the target location as its lowest point. From that point it rises, in terrain steps of steadily increasing height, as we move radially outward from the target in all directions. Terrain Profile step heights are defined such that the actual terrain heights are always below the surface. The Terrain Profile Surface thus guards against short-range irradiation of elevated terrain areas under the laser-target vector. It is used in the CALCZONE module, to aid in the proper definition of the FFLFZ, which can be affected by the underlying terrain step profile.

Following data input, preliminary computations, and definition of the range test scenario to be analysed, the three computational modules mentioned above are executed. The initial module is the Range Boundary Program, known as RBPROG for short. The main purpose of the RBPROG algorithm is to define the Controlled Range Area, which will be used in the CALCZONE module to define the FFLFZ. The CRA is a sub-set of the total Range area, which is “star-shaped” with respect to a given target. A CRA is defined to be star-shaped when any radial, ω , emanating from the target, crosses the Range boundary only once. Frequently the initial Range area does

not satisfy the star-shaped condition, so a portion of it is truncated to form the star-shaped CRA. Extra coordinates are also inserted around the modified CRA boundary to provide appropriate computation points for the CALCZONE algorithm.

The second module, CALCZONE, performs the fault-free laser hazard analysis. Specifically, it calculates the FFLFZ for each designated target within the CRA, and for each designated aircraft altitude. The definition of an FFLFZ begins with a set of radials connecting the target to each of the CRA boundary points. For each radial, ω , emanating from the target, CALCZONE computes a maximum laser firing range-to-target (ground range), $R(\omega)$, such that fault-free laser pointing errors (within the maximum error α_{\max} of the laser-target vector) remain within the CRA. This requirement results in two such ranges-to-target, $R_u(\omega)$ and $R_o(\omega)$, corresponding to the need to keep “undershoot” and “overshoot” laser pointing errors, respectively, within the CRA, as shown in Fig. 2.

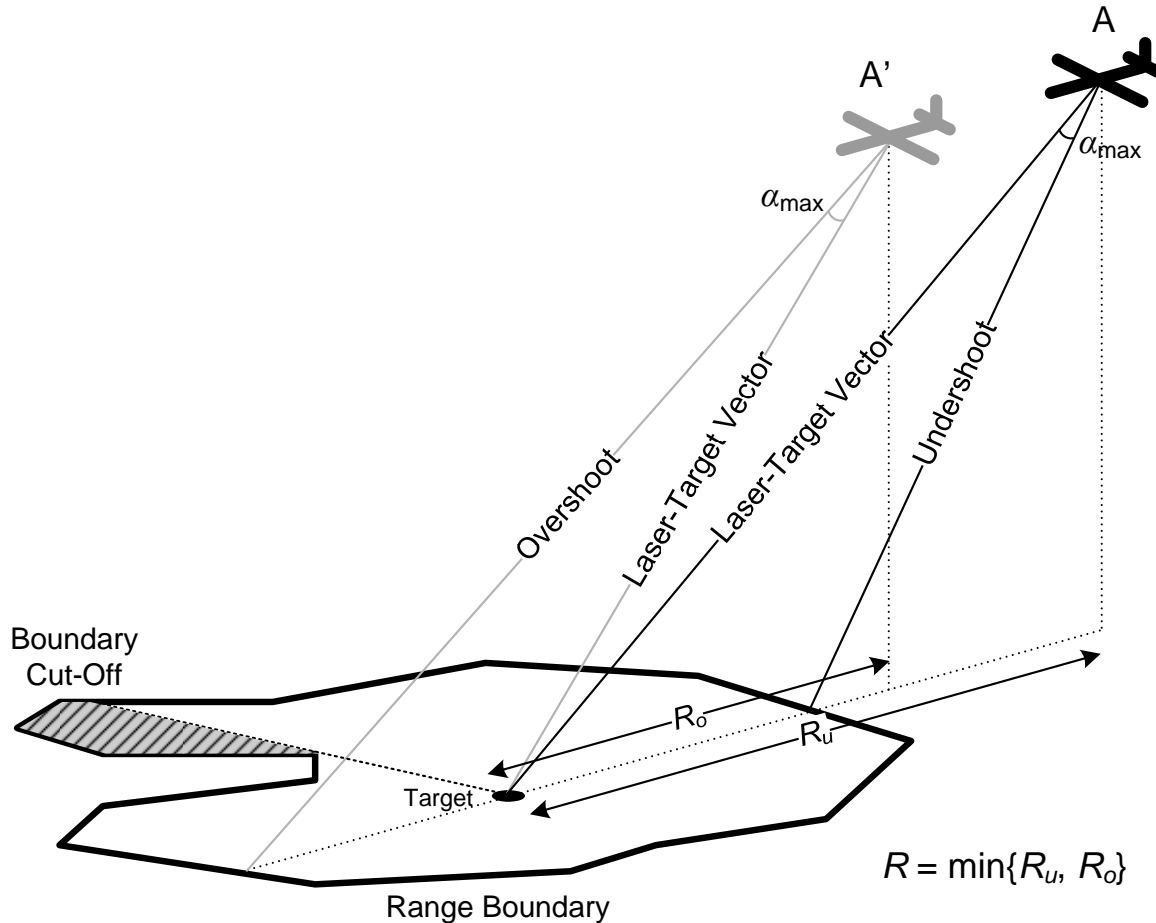


Figure 2: Fault-Free Overshoot & Undershoot

As documented previously [16], the equations for the conditions of undershoot and overshoot ranges do not have analytical solutions, but must be solved by iteration. Once we have calculated the undershoot and overshoot ranges, $R_u(\omega)$ and $R_o(\omega)$, corresponding to aircraft height, H , and to some radial angle, ω , between the target and the near CRA boundary point, the overall maximum firing range, $R(\omega)$, is taken to be the smaller of the two. The FFLFZ for that height can then be defined by calculating the set $\{R(\omega): \omega \in [0, 2\pi)\}$, covering all possible radials to any boundary point. The FFLFZ is typically plotted by laying down each range at the proper radial angle on the map, plotting the end point of each range vector, and then connecting all the end points to make a closed contour about the target. This process is repeated for each proposed attack height. The nested series of contours produced defines a three-dimensional envelope for safe firing of the laser during fault-free operation of the laser directional control system. For any aircraft maneuver, at any given altitude, the FFLFZ defines the maximum range-to-target at which the laser may be fired, assuming fault-free operation of the laser directional controls.

Generation of the FFLFZ contours completes the fault-free laser hazard analysis and lays the foundation for the probabilistic fault/failure hazard analysis performed in CALCFAULT. Prior to execution of CALCFAULT; however, a specific laser attack scenario must be defined. MATILDA provides a feature, the Attack Track Waypoint Editor that allows an analyst to overlay an attack track, defined by a series of waypoints, onto the map. The data entry for waypoints includes waypoint coordinates, aircraft altitude, aircraft velocity, and whether the laser is firing at that waypoint. With this data, MATILDA compares the proposed attack track against the altitude limitations defined by the FFLFZ and indicates to the analyst those portions of the track that are cleared for laser firing and those where laser firing is prohibited. Only the portion of the attack track that clears FFLFZ restrictions is analysed during CALCFAULT execution.

The third module, CALCFAULT, performs the probabilistic fault/failure hazard analysis for the designated and cleared laser attack scenario, to determine if any additional restrictions must be imposed on the laser firing envelope permitted by the FFLFZ. The CALCFAULT analysis quantifies the actual risk for firing along the designated attack track, in the event of a fault in, or a failure of, the laser directional control system. The probabilistic Expectation Model is used in this analysis. Key input parameters for the CALCFAULT analysis include laser system parameters, attack track data, population densities of the Urban Areas surrounding the range (assumed uniform and outside buildings), the terrain computational grid (points on the ground for which ocular damage probability is computed), and of course, the maximum acceptable value of the overall expectation value, $E_{MOVLMAX}$.

Since a fault/failure could occur at any point during the course of the cleared laser attack scenario, a large number of failure cases, each representing a possible failure of the directional control system at a different point along the attack track, must potentially be evaluated and their overall expectation values compared to the Primary Criterion. Generally, the number of failure cases evaluated is equal to the number of pulses fired during the attack scenario; i.e., the fault hazard analysis is performed for a possible failure at each of the laser firing positions. For each laser pulse emitted after the fault/failure, the CALCFAULT algorithm evaluates a corresponding expectation value, e_{MOVL} , that a MOVL will occur in the unprotected population surrounding the CRA.

The number of pulses emitted after a fault or failure has occurred depends on the pulse repetition frequency and the length of time required for the laser to cease firing. Consequently, the overall expectation value, E_{MOVL} , for a particular failure case, is the sum of the individual pulse e_{MOVL} values for the period of time during which the laser continues to fire, and before laser firing is inhibited. Restrictions on laser firing are subsequently imposed on those portions of the aircraft attack track for which the calculated value of E_{MOVL} exceeds the acceptable limit, E_{MOVLMAX} . Additional laser firing restrictions may also be imposed on those portions of the aircraft maneuver that bring the laser to within the applicable MSD of potentially unprotected populated areas.

Summarizing the material of Section 2.2, hazard analyses done with the Smooth Earth TIALD Model require six main computational steps, performed sequentially, using three major computational modules: RBPROG, CALCZONE, and CALCFAULT. The initial step consists of data input, data transformations, generation of the Terrain Profile Surface, and definition of the range test scenario to be analysed. Second, the RBPROG module is executed to generate the CRA and all range boundary points necessary to support the CALCZONE computations. Third, the CALCZONE module is executed, generating the FFLFZ for every specified aircraft attack height. Fourth, an aircraft attack track is generated, including proposed laser firing positions, and compared to the appropriate FFLFZ restrictions. The attack track is then modified to exclude those portions of the track where laser firing is prohibited by the FFLFZ. Fifth, the CALCFAULT module is executed to perform the probabilistic fault/failure hazard analysis for the designated and cleared laser attack track. Based on the analysis additional restrictions may be imposed on the laser firing envelope permitted by the FFLFZ. Sixth and last, the Secondary and Tertiary Precautions are applied to identify any final restrictions on the laser firing envelope.

2.3 MATILDA Version-2.0.3 and the Rough Earth TIALD Model

In the advanced version of MATILDA, MATILDA Version-2.0.3, the Partition/Expectation Model is implemented by means of a Computational Model known as the Rough Earth TIALD Model, which has more complex PRA algorithms appropriate for hilly terrain. Here we give a brief overview and summary of the main computational steps performed, and the major computational modules executed, when hazard analyses are done with the Rough Earth TIALD Model. This overview is intended as a preliminary modelling approach description to those in later Sections, which give detailed documentation of the mathematical algorithms and computational procedures of the major computational modules of the Rough Earth TIALD Model.

Hazard analyses done with the Rough Earth TIALD Model require seven main computational steps, performed sequentially, using four major computational modules: 3D-RBPROG, 3D-CALCZONE, 3D-CALCTERT, and 3D-CALCFAULT. Once again, the initial step consists of data input, data transformations, generation of the Terrain Profile Surface, and definition of the range test scenario to be analysed. Second, the three dimensional RBPROG module (3D-RBPROG) is executed. This consists of executing the two dimensional RBPROG module, to generate the CRA and all range boundary points, and then creating a three dimensional range boundary (3D-CRA) by assigning an elevation to each boundary point. The elevations assigned are equal to the height of the Terrain Profile Step immediately above the boundary point. Third, the new three-dimensional CALCZONE module (3D-CALCZONE) is executed, generating the FFLFZ in hilly terrain for no-fault laser operations. A new method, the Circle of Allowed Laser

Firing (CALF), is used to determine the FFLFZ in hilly terrain. Unlike the old method, the CALF does not require iterative calculations, producing increased computational efficiency. Once again a FFLFZ is generated for every specified aircraft attack height.

Fourth, the new three-dimensional Tertiary Precaution module (3D-CALCTERT) is executed, which modifies the FFLFZ produced by 3D-CALCZONE to mitigate hazards from low probability/high consequence events. Once again the CALF method is applied, this time to produce FFLFZ restrictions arising from the Tertiary Precaution. Fifth, an aircraft attack track is generated and modified, if necessary, to conform to the appropriate FFLFZ restrictions. Sixth, the new three-dimensional CALCFAULT module (3D-CALCFAULT) is executed, to perform probabilistic fault/failure hazard calculations for the cleared laser attack track in hilly terrain. In 3D-CALCFAULT the probabilistic hazard calculation is changed from one performed in the Ground Plane of the target, using Cartesian Coordinates, to one performed in the Display Plane of the aircraft, using Spherical Coordinates. This produces simplification of the algorithms and increased efficiency and speed of computation. Once again, the analysis may impose additional restrictions on the FFLFZ laser firing envelope. Seventh and last, the Secondary Precaution is applied to identify any final restrictions on the laser firing envelope.

3 CALCFAULT: REVISED GROUND PLANE COMPUTATION

As mentioned previously, since 2012 some revisions have been made in the algorithms for the CALCFAULT module, which performs the probabilistic hazard evaluation for the fault/failure condition in the Ground Plane of the target, using Cartesian Coordinates. The basic CALCFAULT computational algorithms, described in our first Technical Report [16], are unchanged; but revisions have been made to the computational algorithms for ground plane evaluation of the single pulse expectation value, e_{MOVL} . This algorithm provides the expectation value that a MOVL will occur, in the unprotected population surrounding the CRA, due to a single laser pulse that escapes the CRA during a fault/failure condition. The revisions were necessary to ensure compatibility with the computational algorithms for display plane evaluation of e_{MOVL} , which are presented in Section 4. The revisions relate to the form and derivation of the Jacobian function used to transform the fault laser pointing error Probability Distribution Function (PDF), $f(\theta, \phi)$, in the aircraft display plane, to the PDF of the ground-projected fault laser pointing errors, used in the ground-plane evaluation.

3.1 CALCFAULT Computation in the Ground Plane

As summarized in Section 2.2, CALCFAULT performs the probabilistic fault/failure hazard analysis for the designated and cleared laser attack scenario. Since a fault/failure could occur at any point during the course of the cleared attack scenario, the fault hazard analysis is performed for a possible failure at each of the laser firing positions. For each laser pulse emitted after the fault/failure, the CALCFAULT algorithm evaluates a corresponding single pulse expectation value, e_{MOVL} , that a MOVL will occur due to that pulse escaping the CRA. The overall expectation value, E_{MOVL} , for a particular failure case, is thus the sum of the individual pulse e_{MOVL} values for all pulses emitted during the failure event. Restrictions on laser firing are subsequently

imposed on those portions of the attack track for which the calculated value of E_{MOVL} exceeds the acceptable limit, E_{MOVLMAX} .

The overall expectation value, $E_{\text{MOVL}}(i)$, of an unprotected observer sustaining a MOVL as a result of a fault/failure occurring on the i -th pulse emitted during laser firing operations is given by [16]

$$E_{\text{MOVL}}(i) = P_F \sum_{j=0}^{m-1} e_{\text{MOVL}}(i+j), \quad (3.1)$$

where P_F is the probability of a fault occurring on the i -th pulse, m is the maximum number of pulses emitted during a fault, and $e_{\text{MOVL}}(i)$ is the expectation value of an unprotected observer sustaining a MOVL as a result of the i -th pulse. For a ground plane evaluation, the single pulse expectation value is given by [20]

$$\begin{aligned} e_{\text{MOVL}} &= E[g(\Theta, \Phi)] \\ &= \iint_D f(\theta, \phi) g(\theta, \phi) dA \\ &= \iint_D f_G(x(\theta, \phi), y(\theta, \phi)) g(x(\theta, \phi), y(\theta, \phi)) dx dy \quad , \\ &= \iint_D f(x(\theta, \phi), y(\theta, \phi)) g(x(\theta, \phi), y(\theta, \phi)) |J| dx dy \end{aligned} \quad (3.2)$$

where D is the range of laser sightline directions over which the integral is evaluated, dA is the elemental generic surface area over which the integration is performed, $f(\theta, \phi)$ is the PDF representing the fault laser pointing error relative to the aircraft display plane, the laser sightline error relative to the laser-target vector is defined by the angles (θ, ϕ) , and

$$g(\theta, \phi) = NQ[W_{\text{MOVL}}(h(\theta, \phi))] \quad (3.3)$$

is the expected number of observers sustaining a MOVL if irradiated by a pulse emitted in the direction (θ, ϕ) . In Eq. 3.3

$$N = \rho S_e \quad (3.4)$$

is the expected number of observers irradiated by laser energy within the beam footprint of the errant pulse, evaluated as a function of the beam footprint area S_e and the local population density ρ , and the probability that the observer irradiated sustains a MOVL is represented by the function Q , where

$$Q[x] = \frac{1}{\sqrt{2\pi}} \int_x^\infty e^{-\frac{t^2}{2}} dt \quad (3.5)$$

is the upper-tail of the cumulative standard normal distribution function $N(0,1)$, and the lower limit x is given by

$$W_{\text{MOVL}}(h(\theta, \phi)) = \frac{A \left(-\log_e h(\theta, \phi) + \frac{\eta^2}{2} \right) + B}{\sqrt{1 + A^2 \eta^2}} \quad (3.6)$$

In Eq. 3.6, $A=1.715$, $\eta=1.1$, $B=14.035$ for unaided viewing and $h(\theta, \phi)$ is the laser energy density at the observer assuming *in vacuo* propagation of the laser beam. The ground-projected beam footprint area S_e is given by

$$S_e = S \csc \varphi, \quad (3.7)$$

where

$$\varphi = \tan^{-1} \left(\frac{z_A}{\sqrt{(x_A - x)^2 + (y_A - y)^2}} \right) \quad (3.8)$$

is the elevation angle of the aircraft, located at $A = (x_A, y_A, z_A)$, from the observer location $P = (x, y, z)$.

3.2 Single Pulse Expectation Value: Ground Plane Computation

In Eq. 3.2, the first integral given for the single pulse expectation value is generic, in that it provides no specific reference to the geometric space in which the integral is to be evaluated. In this case we wish to perform an evaluation in the ground plane of the target, using Cartesian coordinates, and assuming a Flat Earth. The Cartesian coordinates are those of the MATILDA Internal Coordinate System (MICS) mentioned earlier [16]. The relationship between a laser pointing error (θ, ϕ) and the corresponding ground plane point (x, y) where the errant pulse strikes will need to be determined, and the generic elemental surface area dA must also be defined in terms of the ground-plane evaluation.

The second integral given in Eq. 3.2 represents the expectation value for the ground plane evaluation

$$e_{\text{MOVL}} = \iint f_G(x(\theta, \phi), y(\theta, \phi)) g(x(\theta, \phi), y(\theta, \phi)) dx dy, \quad (3.9)$$

where $f_G(x(\theta, \phi), y(\theta, \phi))$ is the PDF of the ground-projected fault laser pointing errors. As indicated by the third integral in Eq. 3.2, the PDF of the ground-projected fault laser pointing

errors is obtained by using a Jacobian function to transform the PDF of the display plane fault laser pointing errors [20]:

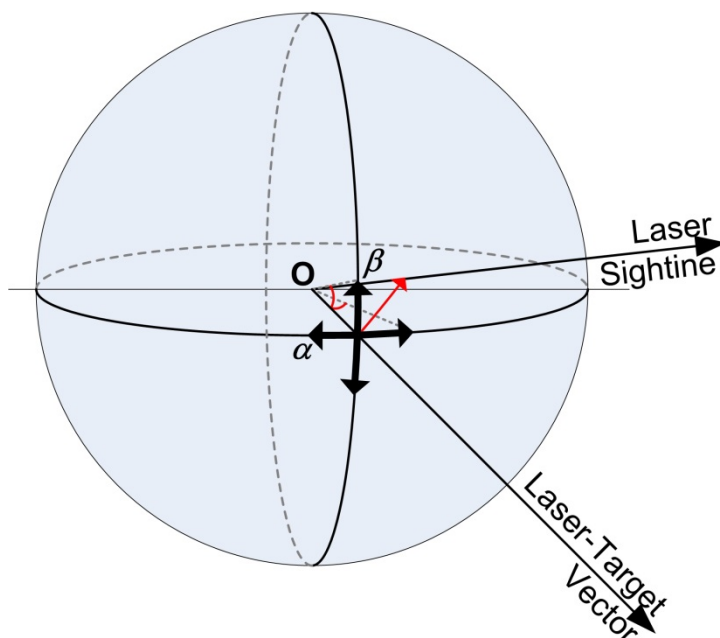
$$f_G(\theta, \phi) = f(\theta, \phi) |J(\theta, \phi)| \quad (3.10)$$

An analytic form for $f_G(x(\theta, \phi), y(\theta, \phi))g(x(\theta, \phi), y(\theta, \phi))$ is generally not available, so that the integral must be evaluated numerically.

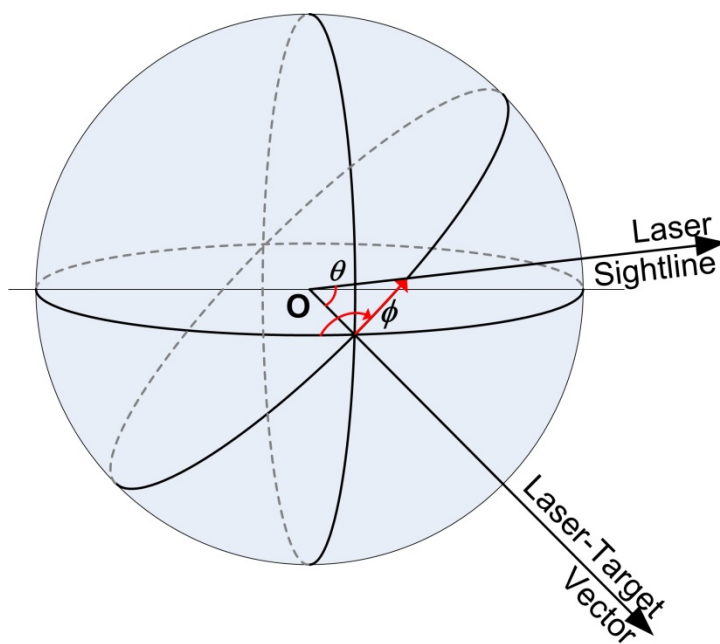
In the remainder of Section 3 we define the algorithms required for ground plane evaluation of the single pulse expectation value. In Section 3.3 we discuss two different display plane coordinate systems: a radial coordinate system, producing the set of radial laser pointing errors (θ, ϕ) , and an orthogonal coordinate system, producing the set of orthogonal laser pointing errors (α, β) . Each of the two forms is useful for different applications. In Section 3.4 we define the colatitude and longitude angles (θ, ϕ) , for an errant laser pulse striking an arbitrary MICS ground plane point (x, y) . In Section 3.5 we define the laser pointing error PDF, $f(\theta, \phi)$, in the display plane, which is most conveniently done in a radial coordinate system. In Section 3.6 we define the Jacobian function that transforms the display plane pointing error PDF to the ground-projected pointing error PDF. This is a function most conveniently derived on the basis of an orthogonal (α, β) coordinate system. Finally, in Section 3.7 we discuss the numerical evaluation method for the integral in Eq. 3.9. Before proceeding we should note that the material of Sections 3.3 to 3.7 is only a condensed summary of the far more extensive documentation produced earlier by Dr. Brian Flemming, the TIALD model developer [20]. Readers are directed to earlier documentation for more mathematical detail and some derivations.

3.3 Display Plane Coordinate Systems for Laser Pointing Errors

There are two different ways in which laser pointing errors in the display plane can be expressed relative to the laser-target vector. As mentioned above, these arise from the use of two different display plane coordinate systems: an orthogonal coordinate system, illustrated in Fig. 3(a), which produces the set of orthogonal laser pointing errors (α, β) , and a radial coordinate system,



(a) Orthogonal Pointing Error Model



(b) Radial Pointing Error Model

Figure 3: Laser Pointing Error Coordinate Systems

illustrated in Fig. 3(b), which produces the set of radial laser pointing errors (θ, ϕ) . Both coordinate systems are alternative variations of a spherical latitude-longitude (lat-long) model.

The orthogonal coordinate system is best illustrated in terms of an equatorial model in which the laser – target vector points out from the centre of the sphere through the intersection of the equator and the Greenwich prime meridian, as shown in Fig. 3(a). In this model the azimuth axis is oriented with the equator while the elevation axis is aligned with the prime meridian. An arbitrary laser sightline direction can hence be characterised in terms of a “lat-long” pointing error (α, β) relative to the orthogonal axes, in which β is the latitude (elevation) measured from the equator along the prime meridian, and α is the longitude (azimuth) measured from the prime meridian along the equator.

In the radial coordinate system, the radial laser pointing errors (θ, ϕ) are most familiarly visualised in terms of a polar model, in which the laser – target vector points out from the centre of the sphere through one of the poles. In this approach, the radial position of the laser sightline (the elevation angle θ) would correspond to an angular displacement along one of the meridians, while the sightline bearing (the azimuth angle ϕ) would be the angle between that meridian and the prime meridian. However, spherical symmetry means that the laser – target vector can also point out through the intersection of the Greenwich prime meridian and the equator, as shown in Fig. 3(b). In this case, the laser sightline radial displacement will be along a great circle, while the sightline bearing angle would be measured to the equator.

Both coordinate systems can be useful, and the analyst can adopt whichever approach is more appropriate for the evaluation being carried out. The equations for evaluation of the single pulse expectation value are typically given in terms of the radial pointing errors (θ, ϕ) , as in Eqs. 3.2 to 3.10, due to the fact that the laser pointing error PDF in the display plane, $f(\theta, \phi)$, is most conveniently expressed in the radial coordinate system. The laser pointing error distribution in the display plane is best considered in terms of a spherical model, where the probability that a laser pointing error will occur in a particular angular interval is given by an integration over a spherical area dS . The analytical evaluation of spherical area is onerous in an orthogonal coordinate system, which is why most derivations of the display plane pointing error PDF use a polar coordinate system and radial pointing errors.

Logically, a radial form of the display plane pointing error PDF should be transformed into a ground plane projected pointing error PDF by a Jacobian function derived in radial coordinates, as shown in Eq. 3.10. Here, however, a problem arises. A radial coordinate derivation leads to singularities in the Jacobian of the ground plane transformation [20]. The orthogonal coordinate derivation does not have this problem, and so is the preferred approach. This raises the problem of how to resolve the discrepancy between a display plane pointing error PDF, expressed in terms of the radial pointing errors (θ, ϕ) , and a Jacobian expressed in terms of the orthogonal pointing errors (α, β) . For a general case, with a non-uniform display plane pointing error PDF, this problem has no clear solution, which is why evaluation of the single pulse expectation value in the display plane, discussed in Section 4, is preferred. For display plane evaluation no Jacobian transformation is needed, and any form of the display plane pointing error PDF, uniform or non-uniform, can be used.

A solution to this problem is possible for the ground plane evaluation, however, for the special case of a circularly-symmetric uniform pointing error distribution. In this case it can be shown that a uniform pointing error distribution generated in one coordinate system is equivalent to that generated in another [20], and we have

$$f(\alpha, \beta) = f(\theta, \phi) . \quad (3.11)$$

For this special case, the display plane pointing error PDF, $f(\theta, \phi)$, can indeed be transformed by a Jacobian expressed in terms of the orthogonal pointing errors (α, β) . Over the remainder of Section 3, therefore, we will define the algorithms for the ground plane evaluation of the single pulse expectation value, with the caveat that they apply to the case of a uniform pointing error distribution only. We will use radial coordinates, and radial laser pointing errors (θ, ϕ) , except in Section 3.6, where we derive the Jacobian function in the orthogonal (α, β) coordinate system.

3.4 Colatitude and Longitudinal Angles

Since we work primarily in radial coordinates, a good starting point for the ground plane evaluation is to define the colatitude and longitude angles (θ, ϕ) , for an errant laser pulse striking an arbitrary MICS ground plane point P . Two Cartesian coordinate systems, with their origins at the target in the ground plane, will be used for this analysis [20]: the MICS with axes (x, y, z) and an “aircraft display” system with axes (x_D, y_D, z_D) . The geometry of the aircraft position relative to the MICS axes is shown in Fig. 4, where the aircraft position relative to the target T in MICS is defined by its position vector $A = (x_A, y_A, z_A)$, x_A and y_A are the MICS eastings and northings of the aircraft, respectively, and z_A is the MICS height of the aircraft above the target.

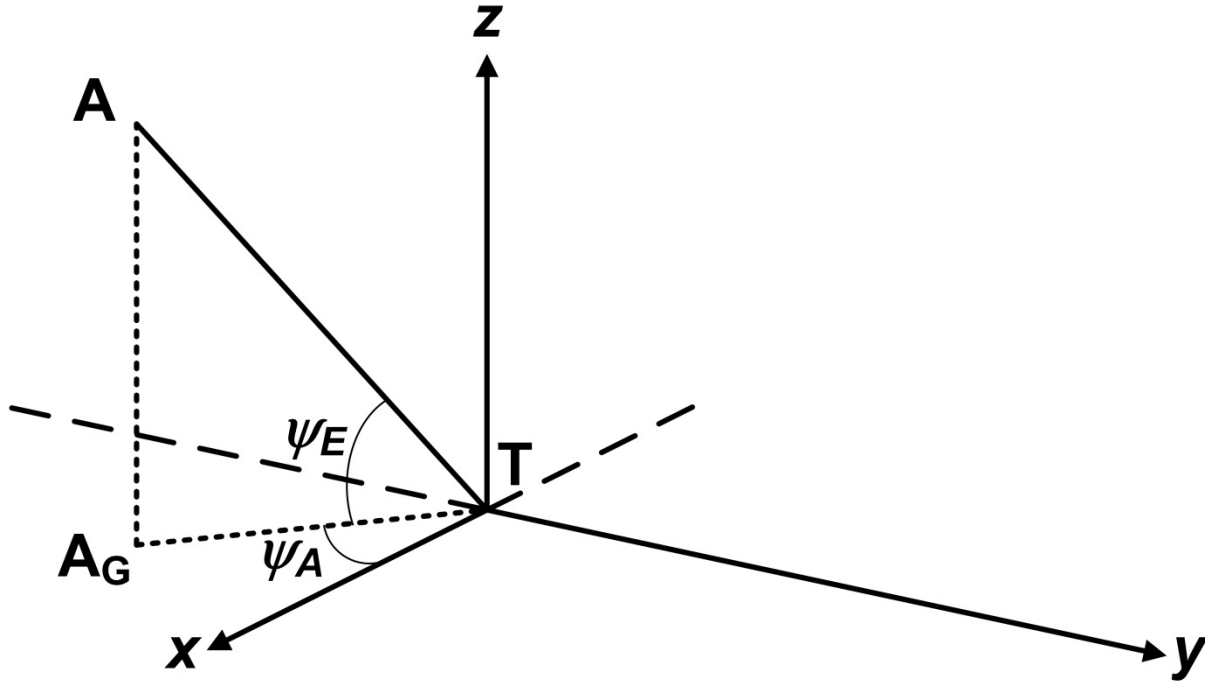


Figure 4: Aircraft - Target Geometry

Note that the azimuth angle ψ_A is defined relative to the *positive MICS x-axis*, and is given by

$$\psi_A = \begin{cases} \tan^{-1} \frac{y_A}{x_A} & x_A \geq 0 \\ \frac{\pi}{2} + \tan^{-1} \frac{y_A}{x_A} & x_A < 0 \quad y_A \geq 0. \\ -\frac{\pi}{2} + \tan^{-1} \frac{y_A}{x_A} & x_A < 0 \quad y_A < 0 \end{cases} \quad (3.12)$$

The elevation angle ψ_E is given by

$$\psi_E = \sin^{-1} \left(\frac{z_A}{\sqrt{x_A^2 + y_A^2 + z_A^2}} \right). \quad (3.13)$$

The aircraft display plane axes relative to the MICS are shown in Fig. 5.

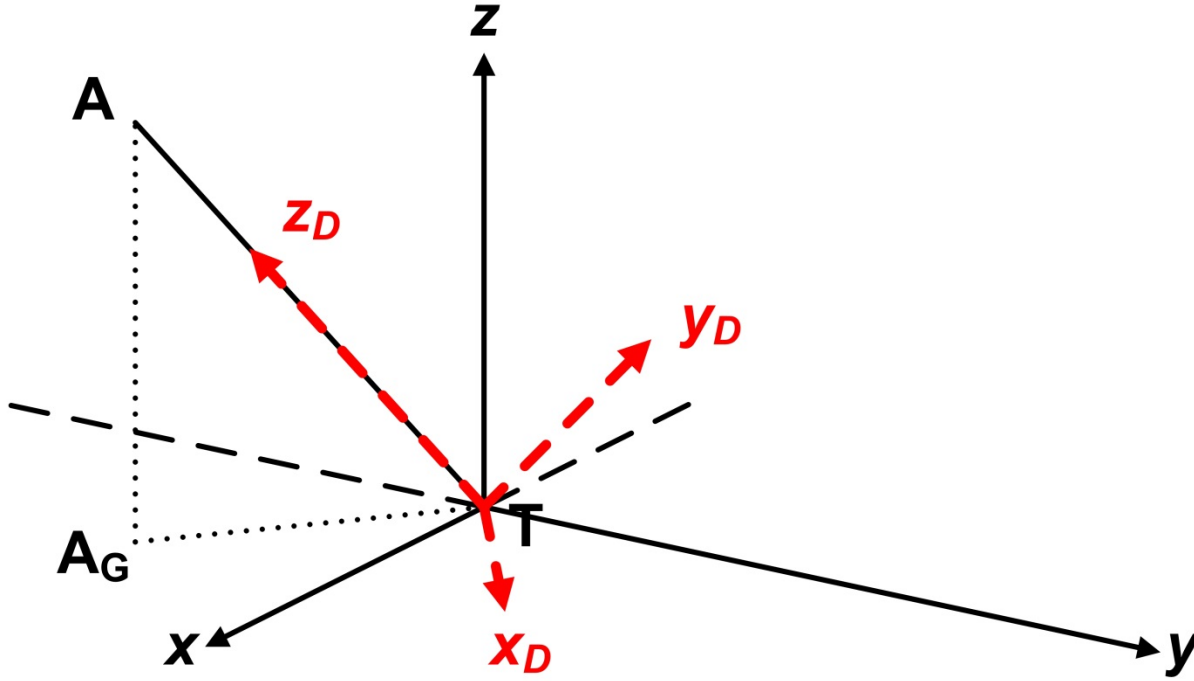


Figure 5: Aircraft Display Axes

To obtain the aircraft display axes, the MICS axes must be rotated so that the z_D -axis is pointing directly towards the aircraft, and the x_D and y_D display axes are pointing upwards and rightwards, respectively, as seen from the perspective of the laser system operator. The axes rotation may be carried in a single operation by the combination of two rotations:

- a rotation about the MICS z -axis through an angle $\left(\psi_A + \frac{\pi}{2}\right)$
- a rotation about the local display x_D axis through an angle $\left(\frac{\pi}{2} - \psi_E\right)$.

Thus, if the MICS x , y , and z -axes are represented by the unit vectors $[1, 0, 0]$, $[0, 1, 0]$, and $[0, 0, 1]$, respectively, then the unit vectors in the local display axes are given by:

$$\hat{x}_D = \begin{bmatrix} -\sin \psi_A \\ \cos \psi_A \\ 0 \end{bmatrix} \quad (3.14)$$

(3.15)

$$(3.16)$$

The geometry of an arbitrary point $P = (x_p, y_p, z_p)$ in the ground-plane is illustrated in Fig.6.

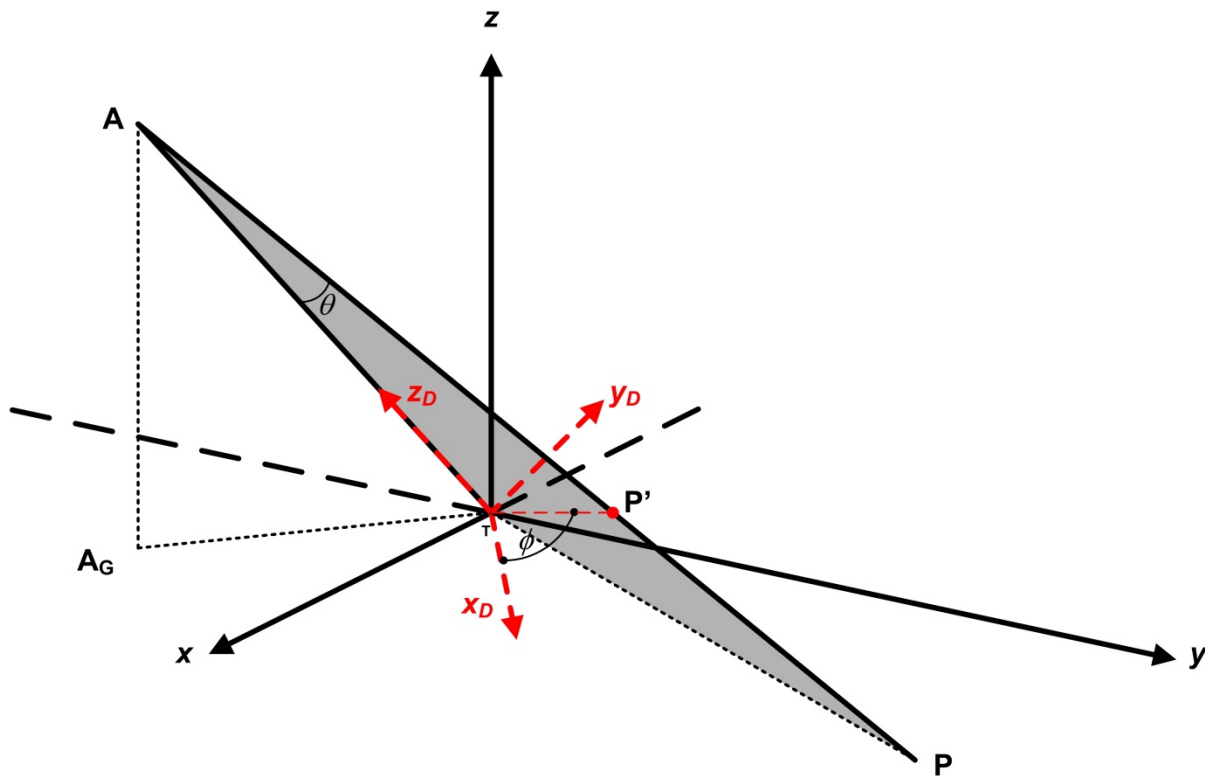


Figure 6: Colatitude and Longitude

The colatitude angle θ is the angle between the laser – target vector AT (i.e. the negative z axis) and the laser Line of Sight (LOS) to the point P , represented by the vector AP, and is obtained through use of the dot product, so that

$$\theta = \cos^{-1} \left(\frac{AT \cdot AP}{\|AT\| \|AP\|} \right) , \quad (3.17)$$

where $\|AT\|$ and $\|AP\|$ are the magnitudes (lengths) of the vectors AT and AP , respectively, and the open rectangle represents a dot product. The longitude ϕ is the angle between the local x_D display axis and the projection TP' of the vector TP in the display axes (x_D, y_D) plane, where TP is the vector between the target and the ground-point P . A clearer illustration of the geometry of the point P' and its' relation to the longitude is provided in Fig. 7.

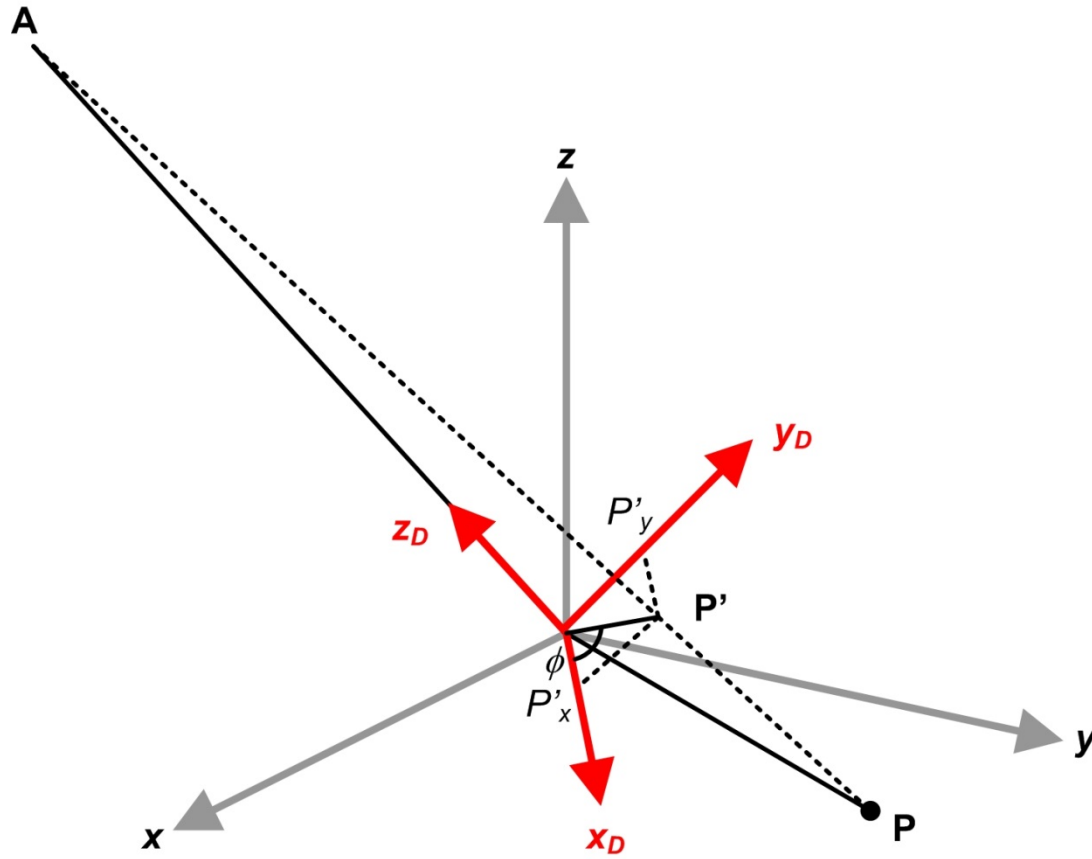


Figure 7: Longitude

From the diagram, the length of the vector TP' is

$$\|TP'\| = \|AT\| \tan \theta , \quad (3.18)$$

and the length of the vector AP' is

$$\|AP'\| = \frac{\|AT\|}{\cos \theta} \quad , \quad (3.19)$$

so that the coordinates of $P' = (x_{P'}, y_{P'}, z_{P'})$ can be determined from the set of parametric equations

$$\begin{aligned} x_{P'} &= x_A + t(x_P - x_A) \\ y_{P'} &= y_A + t(y_P - y_A) \\ z_{P'} &= z_A + t(z_P - z_A) \end{aligned} \quad (3.20)$$

where

$$t = \frac{\|AT\|}{\|AP\| \cos \theta} \quad . \quad (3.21)$$

The angles (η, ς) that the projection TP' makes with the display axes x_D and y_D are given by

$$\eta = \cos^{-1} \left(\frac{P' \cdot x_D}{\|P'\| \|x_D\|} \right) \quad (3.22)$$

and

$$\varsigma = \cos^{-1} \left(\frac{P' \cdot y_D}{\|P'\| \|y_D\|} \right) \quad , \quad (3.23)$$

respectively. Hence, the required longitudinal angle ϕ is given by

$$\phi = \begin{cases} \eta & \text{for } 0 \leq \eta \leq \pi \quad \text{and} \quad 0 \leq \varsigma \leq \frac{\pi}{2} \\ -\eta & \text{for } 0 < \eta < \pi \quad \text{and} \quad \frac{\pi}{2} < \varsigma \leq \pi \end{cases} \quad . \quad (3.24)$$

The longitude ϕ is set to zero, for computational purposes, in the special case when the ground point P is coincident with the target.

3.5 Laser Pointing Error Distribution Function in the Display Plane

As discussed in Section 3.3, the choice of the display plane coordinate system for the laser pointing error PDF drives the form of the Jacobian needed for the display plane to ground plane transformation given in Eq. 3.10. In theory, either the radial or the orthogonal coordinate system described in Section 3.3 could be used. In practice, the display plane laser pointing error distribution is best considered in terms of a spherical model, using spherical coordinates, where integra-

tion is done over a section of a spherical surface. Since analytical evaluation of a spherical area is onerous in orthogonal coordinates, the problem lends itself naturally to derivation in the radial coordinate system, using the set of radial laser pointing errors (θ, ϕ) derived in Section 3.4.

As shown in Fig. 8, the spherical coordinates of a point S on the surface of a sphere are (r, θ, ϕ) , where r is the radial distance from the origin O , θ is the colatitude angle measured with respect to the positive z axis (i.e. the North pole), and ϕ is the longitudinal angle from the positive x axis.

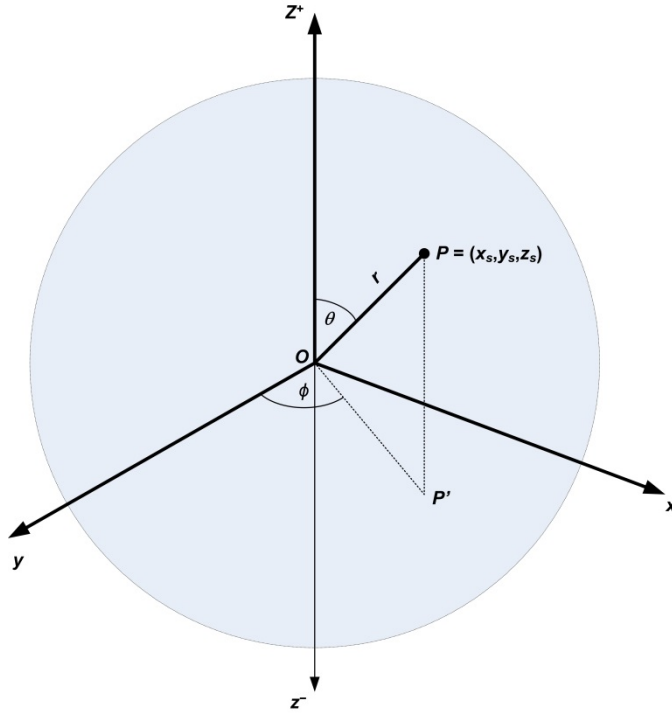


Figure 8: Spherical Coordinate System

The corresponding spherical coordinates (x_s, y_s, z_s) relative to the positive z axis are given by

$$\begin{aligned} x_s &= r \sin \theta \cos \phi \\ y_s &= r \sin \theta \sin \phi \\ z_s &= r \cos \theta \end{aligned} \quad (3.25)$$

For laser hazard analysis purposes it will be convenient to describe the laser pointing errors relative to the *negative* z axis aligned with the laser – target vector. In this case, the point S will have coordinates

$$\begin{aligned}
x_s &= r \sin \mathcal{G} \cos \phi = r \sin \theta \cos \phi \\
y_s &= r \sin \mathcal{G} \sin \phi = r \sin \theta \sin \phi \\
z_s &= r \cos \mathcal{G} = -r \cos \theta
\end{aligned}
\tag{3.26}$$

where $\mathcal{G} = \pi - \theta$ is the colatitude angle relative to the *negative* z axis. The primary difference between Equations 3.25 and 3.26 is that the z_s coordinate, when expressed in terms of the colatitude angle θ , has become negative. Thus, for all practical purposes, the colatitude angle θ can be taken to be measured relative to the laser – target vector and the laser pointing errors can be easily described in terms of a radial (θ, ϕ) model, with random variables Θ and Φ representing the colatitude (polar) and longitude (azimuthal) angles respectively on a unit sphere ($r = 1$).

Assuming a radial pointing error model, Fig. 9 illustrates the probability of a laser pointing error occurring within an elemental angular cone $(\theta + d\theta, \phi + d\phi)$, relative to the laser-to-target vector.

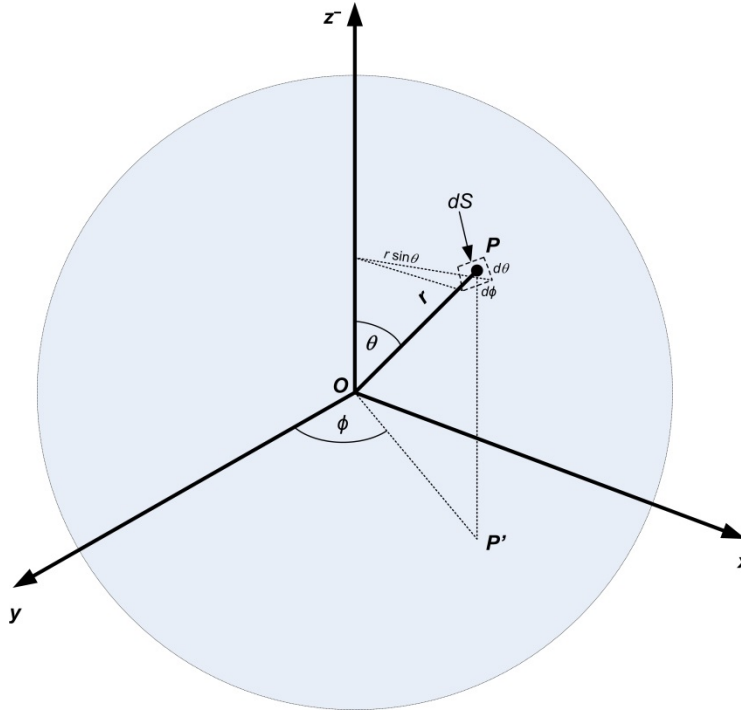


Figure 9: Probability of a Laser Pointing Error

The proportion of laser pointing errors within the elemental range $(\theta + d\theta, \phi + d\phi)$ will also occur in an elemental surface area, dS , where

$$dS = r^2 \sin \theta d\theta d\phi \quad , \quad (3.27)$$

and where $dS = \sin \theta d\theta d\phi$ for a unit sphere ($r = 1$). The presence of the $\sin \theta$ term implies that the size of dS decreases as the polar angle θ approaches the poles at $\theta = 0$ and $\theta = \pi$.

For a given display plane pointing error PDF in radial coordinates, $f(\theta, \phi)$, the corresponding Probability Density Element (PDE) on the surface of the (unit) sphere is $f(\theta, \phi) dS$. From Eq. 3.27 with $r = 1$

$$\begin{aligned} f(\theta, \phi) dS &= f(\theta, \phi) \sin \theta d\theta d\phi \\ &= f_s(\theta, \phi) d\theta d\phi \end{aligned} \quad , \quad (3.28)$$

where $f_s(\theta, \phi)$ is the PDF of pointing errors *on the sphere*, given by

$$f_s(\theta, \phi) = f(\theta, \phi) \sin \theta. \quad (3.29)$$

There are hence two distributions associated with a spherical surface, namely $f(\theta, \phi)$ and $f_s(\theta, \phi)$. While $f(\theta, \phi)$ is the PDF of pointing errors in display axes, $f_s(\theta, \phi)$ is the equivalent PDF on a spherical surface taking into account the distortion introduced in the transformation from a Cartesian to a spherical space.

Now let $f(\theta, \phi)$ represent the fault laser pointing error PDF for pointing in some colatitude direction θ and longitudinal direction ϕ , where the angular ranges are

$$0 \leq \phi < 2\pi \quad \text{and} \quad 0 \leq \theta \leq \theta_{\max} ,$$

and θ_{\max} is the maximum fault laser pointing angle. The probability that a laser pulse will pass through any point located on the surface of the unit spherical sector defined by this angle space is unity. That is:

$$\int_0^{\theta_{\max}} \int_0^{2\pi} f_s(\theta, \phi) d\theta d\phi = \int_0^{\theta_{\max}} \int_0^{2\pi} f(\theta, \phi) \sin \theta d\theta d\phi = 1 \quad . \quad (3.30)$$

Assuming a circularly-symmetric uniform pointing error distribution

$$f(\theta, \phi) = \frac{1}{2\pi(1 - \cos \theta_{\max})} \quad (3.31)$$

gives

$$\int_0^{2\pi} \int_0^{\theta_{\max}} \frac{\sin \theta d\theta d\phi}{2\pi(1 - \cos \theta_{\max})} = \frac{2\pi}{2\pi} \int_0^{\theta_{\max}} \frac{\sin \theta d\theta}{1 - \cos \theta_{\max}} = \frac{[-\cos \theta]_0^{\theta_{\max}}}{1 - \cos \theta_{\max}} = \frac{1 - \cos \theta_{\max}}{1 - \cos \theta_{\max}} = 1 \quad . \quad (3.32)$$

As discussed in Section 3.3, there is a discrepancy between the display plane pointing error PDF, best derived in a radial (θ, ϕ) coordinate system, and the Jacobian for the display plane to ground plane transformation, which must be derived in an orthogonal (α, β) coordinate system to avoid singularities in the function. The discrepancy can be resolved for the ground plane evaluation involving the special case of the circularly-symmetric uniform pointing error distribution given in Eq. 3.31. In this case it can be shown that a uniform pointing error distribution generated in one coordinate system is equivalent to that generated in another [20], giving

$$f(\alpha, \beta) = f(\theta, \phi) \quad .$$

For this special case, the display plane radial pointing error PDF, $f(\theta, \phi)$, can be transformed by a Jacobian expressed in terms of the orthogonal pointing errors (α, β) . We now turn to definition of the Jacobian function in the orthogonal (α, β) coordinate system.

3.6 Jacobian Function in Orthogonal Coordinates

We begin our definition of the Jacobian function with a discussion of the relationship between the display plane orthogonal (α, β) coordinate system, a new ground plane Cartesian coordinate system with axes (u, v, w) oriented to the laser-target vector, the MICS with axes (x, y, z) , and the laser projection geometry from the display plane to the ground plane [20]. The laser projection geometry, relative to the new (u, v, w) coordinate system, is shown in Fig. 10. Like the MICS, the (u, v, w) coordinate system has its origin at the target T in the ground plane, and its vertical w -axis is coincident with the MICS z -axis. The difference between the two Cartesian coordinate systems lies in the orientation of the axes in the ground plane. The MICS positive x and y axes are fixed, and assumed to point east and north, respectively. In contrast, the orientations of the u and v axes vary in time, as a function of the time-varying position of the aircraft and laser. Their orientations, at any particular instant in time, are defined such that the aircraft/laser position at point A , the target T , and the laser-target vector between them all lie in the v - w plane, as shown in Fig. 10.

The illustration also shows the effect of the fault laser pointing error: a laser LOS with angular pointing errors (α, β) relative to the laser-target vector, and striking the ground plane at an arbitrary point $P = (u, v, w)$. The distances between the aircraft and the target, and between the aircraft and the point P , are R_0 and R respectively, and the downwards elevation angle of the laser-to-target vector relative to the local horizontal is ψ_E .

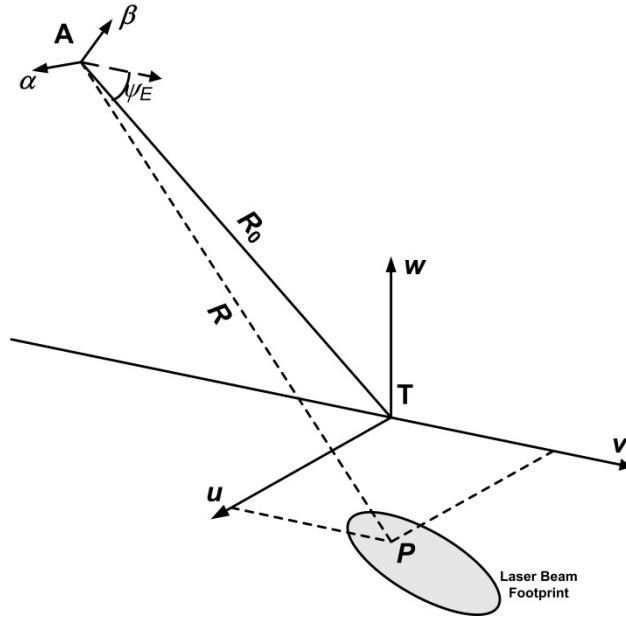


Figure 10: Laser Projection Geometry

Fig. 10 does not indicate the aircraft flight path. The simplest attack track would be one in which the aircraft flies directly at the target, in the direction of the positive v -axis; however, we wish to consider a more general aircraft path, offset to one side of the target, as shown in Fig. 11.

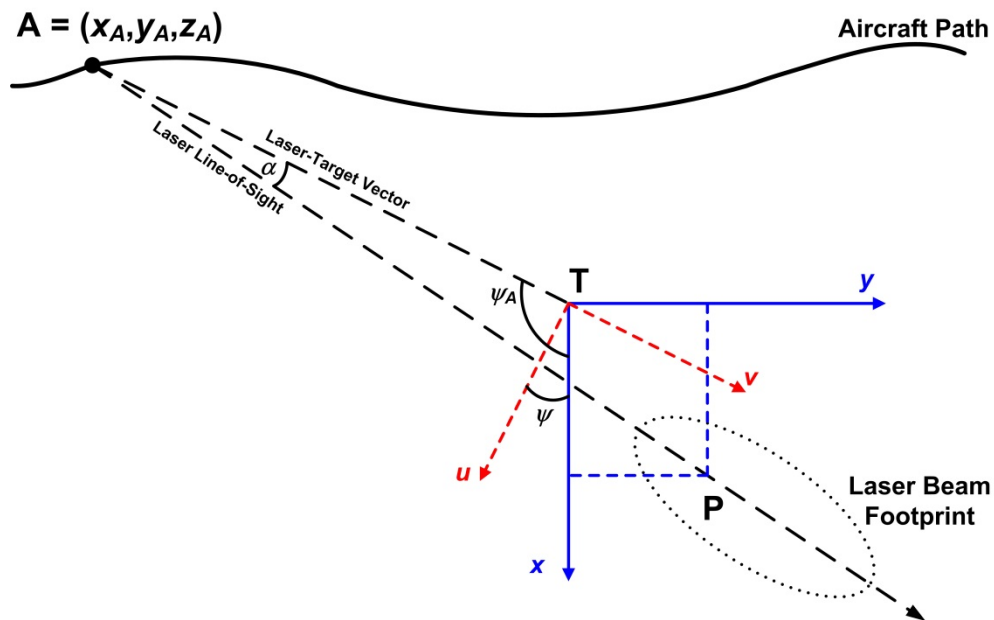


Figure 11: Aircraft Path Geometry

Figure 11 illustrates the aircraft path geometry from above, projected onto the ground plane, and shows the aircraft position relative to both ground plane Cartesian coordinate systems. Once again the laser-target vector lies in the v - w plane. The aircraft position in the MICS is given by $A = (x_A, y_A, z_A)$, where x_A and y_A are the MICS eastings and northings of the aircraft respectively, and z_A is the MICS height of the aircraft above the target. The critical angles shown in Figs.10 and 11 can all be computed from the aircraft MICS coordinates. The aircraft bearing angle ψ_A relative to the *positive MICS x-axis* is given by

$$\psi_A = \begin{cases} \tan^{-1} \frac{y_A}{x_A} & x_A \geq 0 \\ \frac{\pi}{2} + \tan^{-1} \frac{y_A}{x_A} & x_A < 0 \quad y_A \geq 0 \\ -\frac{\pi}{2} + \tan^{-1} \frac{y_A}{x_A} & x_A < 0 \quad y_A < 0 \end{cases} \quad (3.33)$$

The elevation angle ψ_E is given by

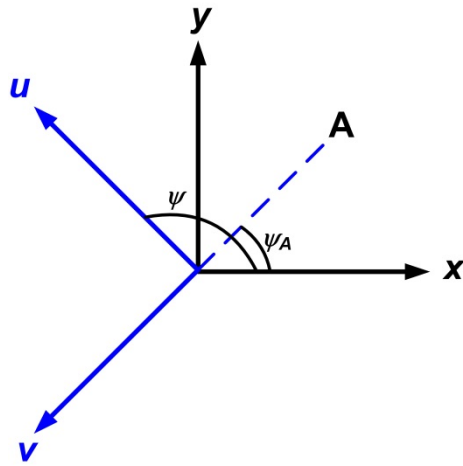
$$\psi_E = \sin^{-1} \left(\frac{z_A}{\sqrt{x_A^2 + y_A^2 + z_A^2}} \right) \quad (3.34)$$

(Note that these expressions are identical to those of Equations 3.12 and 3.13, previously given in Section 3.4.) The (u, v, w) axes are oriented at a rotation angle

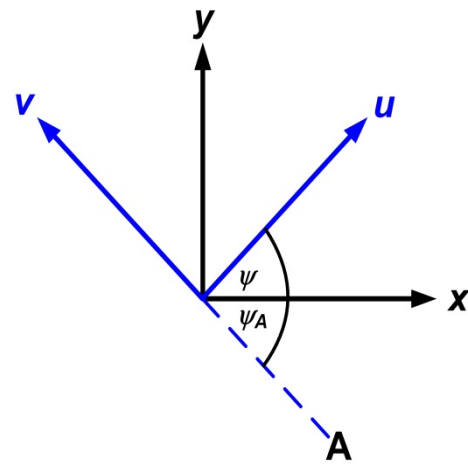
$$\psi = \psi_A + \frac{\pi}{2} \quad (3.35)$$

relative to the MICS (x, y, z) axes.

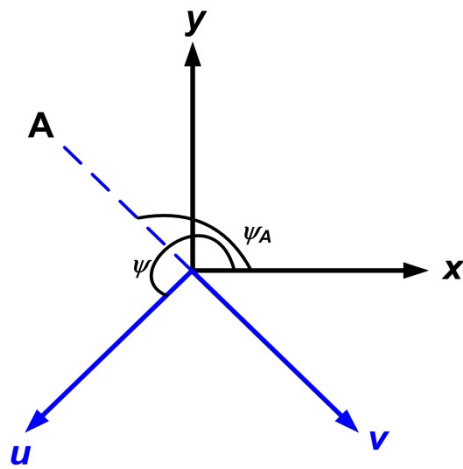
The bearing and rotation angles in Eq. 3.35 can have either positive or negative values, depending on the quadrant in which the aircraft is located and whether the angle represents a counter-clockwise or clockwise rotation from the positive x -axis. The four quadrants in which the aircraft can be located, and the bearing and rotation angles for each, are illustrated in Fig. 12. Comparing these quadrant orientations to that of Fig. 11, we can see that the aircraft there is south-west of the target, and that both the bearing and rotation angles are negative (clockwise rotation with respect to the positive x -axis). A “quadrant-sensitive” value of ψ_A may be evaluated using the “atan2” function that is often included as a standard function in most modern mathematical computation packages.



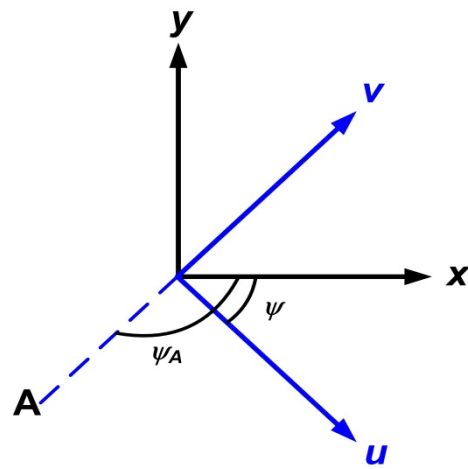
(a) North-East Quadrant



(b) South-East Quadrant



(c) North-West Quadrant



(d) South-West Quadrant

Figure 12: Aircraft Positions in Four Quadrants

A coordinate transformation of the point P from MICS (x, y, z) coordinates to (u, v, w) coordinates, using the rotation angle of Eq. 3.35 gives [20]:

$$\begin{aligned} u &= x \cos \psi + y \sin \psi \\ &= -x \sin \psi_A + y \cos \psi_A \end{aligned} \tag{3.36}$$

and

$$\begin{aligned}
v &= -x \sin \psi + y \cos \psi \\
&= -x \cos \psi_A - y \sin \psi_A
\end{aligned} \tag{3.37}$$

Having examined the relationship between the various coordinate systems, aircraft positions, bearing angles, and the laser projection geometry, it is clear that derivation of a Jacobian expressed in terms of the orthogonal pointing errors (α, β) is best performed using the rotated (u, v, w) coordinate system. Since both the display plane orthogonal (α, β) coordinate system and the ground plane Cartesian (u, v, w) coordinate system are oriented with respect to the laser-target vector, the math is simplified by this choice of coordinates.

Assuming a flat-Earth model, the change of variables theorem allows us to express the display plane orthogonal pointing error PDF, $f(\alpha, \beta)$, the ground-projected pointing error PDF, $f_G(\alpha, \beta)$, and the Jacobian that transforms one to the other, in terms of (u, v) coordinates. Thus, the transformation to the ground-projected pointing error distribution may be expressed as

$$f_G(u, v) = f(\alpha(u, v), \beta(u, v)) |J| \tag{3.38}$$

where

$$|J| = \begin{vmatrix} \frac{\partial \alpha}{\partial u} & \frac{\partial \beta}{\partial u} \\ \frac{\partial \alpha}{\partial v} & \frac{\partial \beta}{\partial v} \end{vmatrix} = \left| \frac{\partial \alpha}{\partial u} \frac{\partial \beta}{\partial v} - \frac{\partial \alpha}{\partial v} \frac{\partial \beta}{\partial u} \right| \tag{3.39}$$

is the determinant of the Jacobian matrix of the partial derivatives of $\alpha(u, v)$ and $\beta(u, v)$ with respect to u and v . The final step in producing the required expression for the Jacobian is thus the derivation of the partial derivatives.

Returning to the laser projection geometry, Fig. 13 illustrates the ground-projected footprint of a circularly-symmetric pointing error cone with a circular cross-section. The ground-projected footprint will be a conic section, as will the footprint of a circularly-symmetric laser beam. Another useful view, shown in Fig. 14, is the projection of the pointing error cone on an orthogonal plane, specifically a plane through T and perpendicular to the laser-target vector.

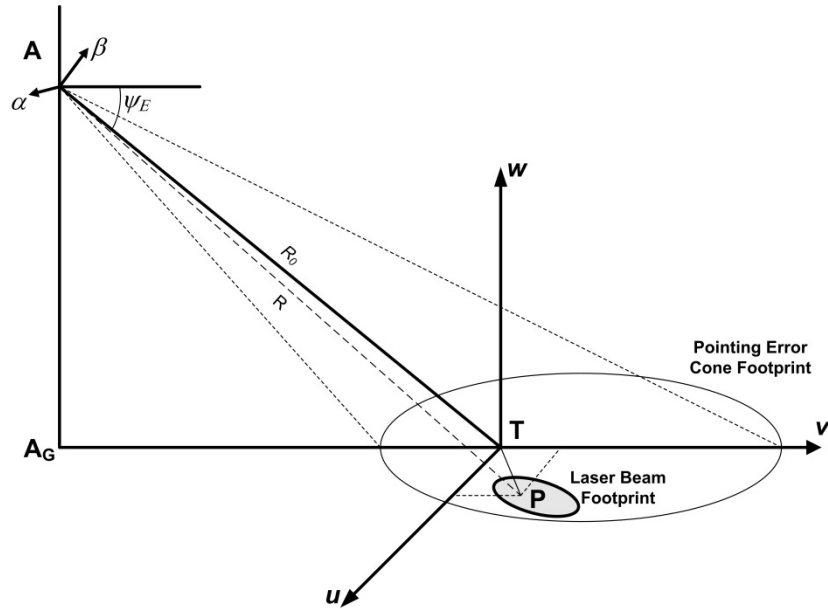


Figure 13: Pointing Error Cone Projection

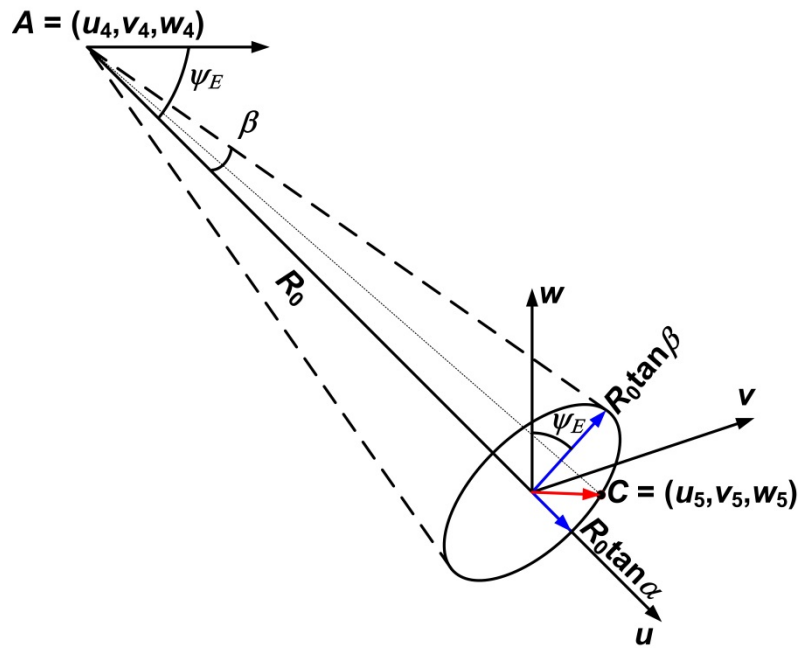


Figure 14: Orthogonal Pointing Error Cone Projection

To determine the projection of the pointing error cone on the ground plane consider an arbitrary laser LOS within the pointing error cone, emanating from the laser source with bearing (α, β) relative to the laser-target vector, and impinging on the ground plane at a point $P = (u, v, w)$. The interception of this laser LOS with the ground plane can be modelled as the interception of a straight line with a flat plane [20]. From Fig. 14, the laser source at the point A has co-ordinates

$$A = (u_4, v_4, w_4) = (0, -R_0 \cos \psi_E, R_0 \sin \psi_E), \quad (3.40)$$

and the co-ordinates of a point C , representing the intersection of the laser LOS with the orthogonal plane, are

$$C = (u_5, v_5, w_5) = (R_0 \tan \alpha, R_0 \tan \beta \sin \psi_E, R_0 \tan \beta \cos \psi_E). \quad (3.41)$$

The co-ordinates of the point $P = (u, v, w)$ in the ground plane are now related to A and C by

$$P = A + t(C - A) \quad (3.42)$$

so that

$$\begin{aligned} u &= u_4 + t(u_5 - u_4) \\ v &= v_4 + t(v_5 - v_4) \\ w &= w_4 + t(w_5 - w_4) \end{aligned} \quad (3.43)$$

From Eqs. 3.40 and 3.41, we have expressions for the (u, v, w) coordinates of A and C in terms of the bearing angles (α, β) , leaving only t undetermined in Eq. 3.43. Since the point P is in the ground plane, however, we can set

$$w = w_4 + t(w_5 - w_4) = 0. \quad (3.44)$$

Solving this for t and inserting the result into Eq. 3.43, we have

$$u = u_4 + t(u_5 - u_4) = -\frac{R_0 \tan \alpha \sin \psi_E}{\tan \beta \cos \psi_E - \sin \psi_E} \quad (3.45)$$

$$v = v_4 + t(v_5 - v_4) = -\frac{R_0 \tan \beta}{\tan \beta \cos \psi_E - \sin \psi_E} \quad (3.46)$$

Now, from Eqs. 3.44 to 3.46 we can obtain

$$\alpha(u, v) = \tan^{-1} \left(\frac{u}{R_0 + v \cos \psi_E} \right) \quad (3.47)$$

and

$$\beta(u, v) = \tan^{-1} \left(\frac{v \sin \psi_E}{R_0 + v \cos \psi_E} \right) \quad (3.48)$$

From these expressions the key partial derivatives are

$$\frac{\partial \alpha}{\partial u} = \frac{R_0 + v \cos \psi_E}{(R_0 + v \cos \psi_E)^2 + u^2} \quad (3.49)$$

and

$$\frac{\partial \beta}{\partial v} = \frac{R_0 \sin \psi_E}{(R_0 + v \cos \psi_E)^2 + v^2 \sin^2 \psi_E} \quad (3.50)$$

Note that, since

$$\frac{\partial \beta}{\partial u} = 0 \quad (3.51)$$

there is no requirement to evaluate $\frac{\partial \alpha}{\partial v}$. The Jacobian of Eq. 3.39 now becomes

$$\begin{aligned} |J| &= \left| \frac{\partial \alpha}{\partial u} \frac{\partial \beta}{\partial v} \right| \\ &= \left| \frac{R_0 (R_0 + v \cos \psi_E) \sin \psi_E}{((R_0 + v \cos \psi_E)^2 + u^2)((R_0 + v \cos \psi_E)^2 + v^2 \sin^2 \psi_E)} \right| \end{aligned} \quad (3.52)$$

and the transformation to the ground-projected pointing error distribution can be written

$$f_G(u, v) = f(\alpha(u, v), \beta(u, v)) \frac{R_0 (R_0 + v \cos \psi_E) \sin \psi_E}{((R_0 + v \cos \psi_E)^2 + u^2)((R_0 + v \cos \psi_E)^2 + v^2 \sin^2 \psi_E)} \quad (3.53)$$

Finally, again using change of variables, the transformation of Eq. 3.53 can also be written in MICS coordinates as

$$\begin{aligned}
f_G(x, y) &= f_G(u(x, y), v(x, y)) \\
&= f(\alpha(u(x, y)), \beta(v(x, y)))|J|
\end{aligned} \tag{3.54}$$

where

$$|J| = \frac{R_0 (R_0 + v(x, y) \cos \psi_E) \sin \psi_E}{\left((R_0 + v(x, y) \cos \psi_E)^2 + u(x, y)^2 \right) \left((R_0 + v(x, y) \cos \psi_E)^2 + v(x, y)^2 \sin^2 \psi_E \right)} \tag{3.55}$$

3.7 Single Pulse Expectation Value: Numerical Evaluation

Our final topic in Section 3 is discussion of a numerical evaluation method for the single pulse expectation value integral given in Eq. 3.9. First, however, as a convenience to the reader, we will give a brief summary of the algorithms already presented in Sections 3.1-3.6, clarifying the order in which these equations are used in the CALCFAULT computational flow. Hopefully, this will help place the numerical evaluation discussion in context, since it is easily possible to lose track of the forest for the trees.

As stated in Section 3.1, CALCFAULT performs the probabilistic fault/failure hazard analysis for a possible failure at each of the laser firing positions on the cleared laser attack. The overall expectation value, E_{MOVL} , of an unprotected observer sustaining a MOVL as a result of a fault/failure occurring on the i -th pulse, is the sum of the single pulse expectation values, e_{MOVL} , for all pulses emitted during the failure event, as given by Eq. 3.1:

$$E_{\text{MOVL}}(i) = P_F \sum_{j=0}^{m-1} e_{\text{MOVL}}(i + j)$$

For a ground plane evaluation, the single pulse expectation value is given by Eq. 3.9:

$$e_{\text{MOVL}} = \iint f_G(x(\theta, \phi), y(\theta, \phi)) g(x(\theta, \phi), y(\theta, \phi)) dx dy$$

Since an analytic form of the integrand $f_G(x(\theta, \phi), y(\theta, \phi)) g(x(\theta, \phi), y(\theta, \phi))$ is not generally available, the integral must be evaluated numerically. In order to do this, we must first be able to numerically evaluate each of the two constituent functions of the integrand, the expected number of observers sustaining a MOVL, $g(\theta, \phi)$, and the ground-projected laser pointing error PDF, $f_G(\theta, \phi)$. Each of these functions must be numerically evaluated for every set of colatitude and longitude angles (θ, ϕ) , corresponding to the laser pointing errors for every MICS ground plane point (x, y) , that might possibly be struck by the errant laser pulse. An array of ground plane points, with sufficient density to give an accurate analysis and covering the projected laser point-

ing error cone, will be chosen by the analyst for each scenario evaluated. Here we summarize the evaluation of the two constituent functions for one arbitrary ground plane point.

We begin with calculation of the aircraft bearing angle, the aircraft elevation angle, and the colatitude and longitude angles (θ, ϕ) , representing an aircraft at position $A = (x_A, y_A, z_A)$ in MICS coordinates, firing a laser pulse that strikes the ground plane point $P = (x_P, y_P, z_P)$. This analysis approach is the calculation presented in Section 3.4. The aircraft bearing angle ψ_A relative to the *positive MICS x-axis* is given by Eq. 3.12:

$$\psi_A = \begin{cases} \tan^{-1} \frac{y_A}{x_A} & x_A \geq 0 \\ \frac{\pi}{2} + \tan^{-1} \frac{y_A}{x_A} & x_A < 0 \quad y_A \geq 0 \\ -\frac{\pi}{2} + \tan^{-1} \frac{y_A}{x_A} & x_A < 0 \quad y_A < 0 \end{cases}$$

The aircraft elevation angle ψ_E is given by Eq. 3.13:

$$\psi_E = \sin^{-1} \left(\frac{z_A}{\sqrt{x_A^2 + y_A^2 + z_A^2}} \right).$$

The colatitude angle θ and the longitudinal angle ϕ are given by Eqs. 3.14-3.17 and 3.20-3.24, respectively, which will not be reproduced here.

Since the computation of the Jacobian is performed in the rotated (u, v, w) coordinates, we use Eq. 3.35 to calculate the rotation angle between the (u, v, w) axes and the MICS (x, y, z) axes:

$$\psi = \psi_A + \frac{\pi}{2}.$$

Using this rotation angle, the coordinate transformation of the point P from MICS (x, y, z) coordinates to (u, v, w) coordinates is now given by Eqs. 3.36 and 3.37:

$$\begin{aligned} u &= x \cos \psi + y \sin \psi \\ &= -x \sin \psi_A + y \cos \psi_A \\ v &= -x \sin \psi + y \cos \psi \\ &= -x \cos \psi_A - y \sin \psi_A \end{aligned}$$

With these preliminary computations complete, we can now numerically evaluate the two constituent functions of the integrand at the ground plane point P . First, the expected number of observers sustaining a MOVL, $g(\theta, \phi)$, is computed from Eq. 3.3

$$g(\theta, \phi) = NQ \left[W_{\text{MOVL}}(h(\theta, \phi)) \right],$$

where the components of $g(\theta, \phi)$ are computed from Eqs. 3.4 - 3.8. Next, the ground-projected laser pointing error PDF $f_G(\theta, \phi)$ is computed from Eq. 3.10

$$f_G(\theta, \phi) = f(\theta, \phi) |J(\theta, \phi)|,$$

where the circularly-symmetric uniform pointing error distribution is given by Eq. 3.31

$$f(\theta, \phi) = \frac{1}{2\pi(1 - \cos \theta_{\max})},$$

and the Jacobian is given by Eq. 3.55

$$|J| = \frac{R_0 (R_0 + v(x, y) \cos \psi_E) \sin \psi_E}{\left((R_0 + v(x, y) \cos \psi_E)^2 + u(x, y)^2 \right) \left((R_0 + v(x, y) \cos \psi_E)^2 + v(x, y)^2 \sin^2 \psi_E \right)}.$$

While the computations above allow us to numerically evaluate the single pulse expectation value integrand at any specified ground plane point, numerical evaluation of the integral requires evaluation of the integrand over *areas* of the ground plane, rather than at single points.

Turning to numerical evaluation methods for integrals, we consider first, as a simple example, the evaluation of an integral of a function $f(x)$, over the single variable x . Evaluation of the integral $Y = \int f(x) dx$ may be thought of as determining the area under the curve $f(x)$. One numerical evaluation method consists of dividing the area under the curve into a series of simpler incremental areas and taking the sum. Each incremental area can be approximated by multiplying the incremental length, $(x_2 - x_1)$, by the mean of the two function values, $f(x_1)$ and $f(x_2)$, at each end of the increment.

Similarly, evaluation of a double integral of a bivariate function $f(x, y)$, over the variables x and y , may be thought of as determining the volume under the surface defined by the function $f(x, y)$. Relating this to Eq. 3.9, the quantity e_{MOVL} is represented by the volume under the surface defined by the bivariate function

$$f_G(x(\theta, \phi), y(\theta, \phi)) g(x(\theta, \phi), y(\theta, \phi))$$

To numerically evaluate the integral we divide this volume into a set of incremental volumes and take the sum. Each incremental volume can be approximated by multiplying the incremental area A by the mean of the four values of $f_G(x(\theta, \phi), y(\theta, \phi))g(x(\theta, \phi), y(\theta, \phi))$ at each corner of the area, as illustrated in Fig. 15.

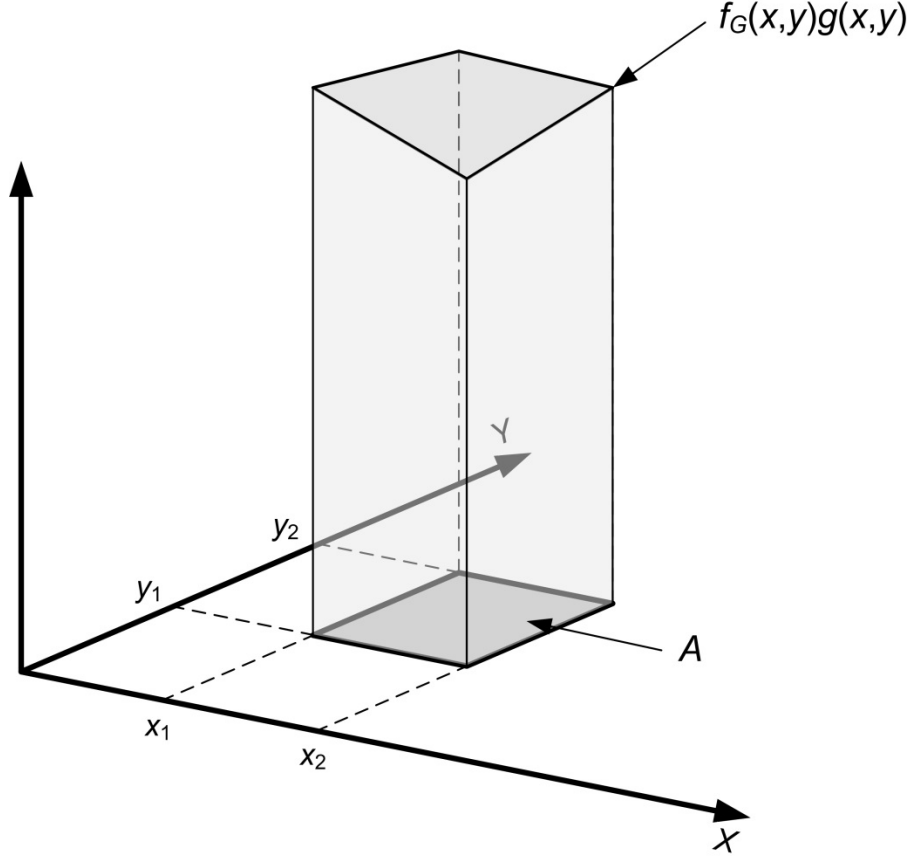


Figure 15: Volume in a Bivariate Integral

Using this method, the integral of Eq. 3.9 can be approximated by the sum

$$e_{\text{MOVL}} \approx A \sum_i \sum_j \bar{f}_G^{(j,i)} \bar{g}^{(j,i)} , \quad (3.56)$$

where

$$\bar{f}_G^{(j,i)} = \frac{(f_G(x_j, y_i) + f_G(x_{j+1}, y_i) + f_G(x_{j+1}, y_{i+1}) + f_G(x_j, y_{i+1}))}{4} , \quad (3.57)$$

and

$$\bar{g}^{(j,i)} = \frac{(g(x_j, y_i) + g(x_{j+1}, y_i) + g(x_{j+1}, y_{i+1}) + g(x_j, y_{i+1}))}{4}, \quad (3.58)$$

respectively, and where

$$A^{(j,i)} = |x_{j+1} - x_j| |y_{i+1} - y_i| = A \quad (3.59)$$

is the elemental area in the ground plane. The summation in Eq. 3.56 is over all quadruplets of adjacent points in the ground plane. For computational purposes, the sample data are presented in a series of spreadsheet arrays in which the rows and columns represent the MICS y and x axes respectively, and (j, i) are the appropriate array column and row indices.

4 3D-CALCFAULT: DISPLAY PLANE COMPUTATION

Having completed documentation of the CALCFAULT computational algorithms for probabilistic fault/failure hazard evaluation in the ground-plane, we now turn to documentation of the computational algorithms for the new 3D-CALCFAULT module, which performs the probabilistic fault/failure hazard evaluation in the Display Plane of the aircraft, using Spherical Coordinates. The shift to probabilistic hazard evaluation in the display plane produces simplification of the algorithms, with increased efficiency and speed of computation, since no Jacobian transformation is needed for display plane evaluation of the single pulse expectation value. Another advantage, mentioned in Section 3.3, is that any form of the display plane pointing error PDF, uniform or non-uniform, can be used for display plane evaluation. (Comparison of the results of the two methods can only be done, however, for the uniform pointing error distribution of Eq. 3.31, which is the special case for which the ground plane algorithms are valid.) Finally, display plane evaluation is better suited for probabilistic hazard evaluation in hilly terrain.

4.1 CALCFAULT Computation in the Display Plane

The computational algorithms for the three-dimensional CALCFAULT (3D-CALCFAULT) module are very similar to those of the old CALCFAULT module, given in Section 3.1, the primary difference being display plane evaluation of the single pulse expectation value. Those equations and computational procedures which are identical will not always be repeated in Section 4; instead, for brevity, some of the Section 3 material will simply be referenced.

As in the old CALCFAULT module, 3D-CALCFAULT only performs the probabilistic fault/failure hazard analysis for the designated and cleared portions of the laser attack track. Once again it is assumed that a fault/failure could occur at any point during the course of the cleared attack scenario, and the fault hazard analysis is performed for a possible failure at each of the laser firing positions. Thus, the overall expectation value, E_{MOVL} , for a particular failure case, is once again the sum of the single pulse expectation values, e_{MOVL} , for all pulses emitted during the failure event, as given by Eq. 3.1

$$E_{\text{MOVL}}(i) = P_F \sum_{j=0}^{m-1} e_{\text{MOVL}}(i+j).$$

For a display plane evaluation, the single pulse expectation value is given by [21]

$$\begin{aligned} e_{\text{MOVL}} &= E[g(\Theta, \Phi)] \\ &= \iint_D f(\theta, \phi) g(\theta, \phi) dS, \\ &= \iint_D f(\theta, \phi) g(\theta, \phi) \sin \theta d\theta d\phi \end{aligned} \quad (4.1)$$

where D is the range of laser sightline directions over which the integral is evaluated, dS is the elemental spherical surface area of integration, $f(\theta, \phi)$ is the PDF representing the fault laser pointing error relative to the aircraft display plane, and the laser sightline error relative to the laser-target vector is once again defined by the colatitude and longitude angles (θ, ϕ) . As before the expected number of observers sustaining a MOVL, $g(\theta, \phi)$ is computed from Eq. 3.3

$$g(\theta, \phi) = NQ[W_{\text{MOVL}}(h(\theta, \phi))],$$

and the components of $g(\theta, \phi)$ are computed from Eqs. 3.4 - 3.8.

Calculation of the aircraft bearing angle, ψ_A , the aircraft elevation angle, ψ_E , and the colatitude and longitude angles (θ, ϕ) , representing an aircraft at position $A = (x_A, y_A, z_A)$ in MICS coordinates, firing a laser pulse that strikes the ground plane point $P = (x_P, y_P, z_P)$, is once again performed using the relationship between the MICS axes (x, y, z) and an “aircraft display” coordinate system with axes (x_D, y_D, z_D) , as previously presented in Section 3.4. The algorithms and computational procedures for these calculations have been given in detail in Section 3.4, and summarized in Section 3.7, so they will not be repeated here.

4.2 Single Pulse Expectation Value: Display Plane Computation

The evaluation of the single pulse expectation value in the display plane is very similar to the ground plane evaluation, except that the integration, or numerical summation when numerical evaluation methods are used, takes place over an elemental spherical surface area on the unit sphere centered on the aircraft, rather than over an elemental surface area in the ground plane. Hence, for the display plane evaluation the single pulse expectation value is given by

$$e_{\text{MOVL}} = \iint f(\theta, \phi) g(\theta, \phi) \sin \theta d\theta d\phi, \quad (4.2)$$

where the elemental spherical surface area on the unit sphere ($r = 1$) is given by

$$dS = \sin \theta d\theta d\phi . \quad (4.3)$$

Once again, an analytic form for the integrand $f(\theta, \phi)g(\theta, \phi)$ is not generally available; thus, the integral must be evaluated numerically. As in the ground plane evaluation, this requires numerical evaluation of the two constituent functions of the integrand, $f(\theta, \phi)$ and $g(\theta, \phi)$, but now we must also numerically evaluate the elemental spherical surface area, a topic dealt with in Section 4.3. Happily, this is a somewhat simpler task than evaluation of the Jacobian. Finally, it should be noted that, between the two evaluation methods,

$$g(\theta, \phi) = g(x(\theta, \phi), y(\theta, \phi)),$$

but

$$f(\theta, \phi) \neq f_G(x(\theta, \phi), y(\theta, \phi)).$$

Over the remainder of Section 4 we define the algorithms required for display plane evaluation of the single pulse expectation value. In Section 4.3 we discuss evaluation of the elemental spherical surface area. In Section 4.4 we discuss the numerical evaluation method for the integral in Eq. 4.2. Finally, Section 4.5 gives a comparison of the ground plane and display plane evaluation methods. Once again we note that the material of Sections 4.3 to 4.5 is only a condensed summary of the more extensive documentation produced earlier by Dr. Brian Flemming, the TIALD model developer [21]. Readers are directed to earlier documentation, discussed and referenced in [21], for more detail.

4.3 Evaluation of Elemental Spherical Surface Area

Evaluation of the elemental spherical surface area requires projection of a grid of four ground plane points, bounding an elemental ground plane surface area, onto the unit sphere centered on the aircraft. This produces a corresponding grid of four display axes points in spherical coordinates, bounding an elemental spherical surface area. An exact analytic expression can be obtained for the spherical surface area bounded by each quadruplet of display axes points and this is the expression required for numerical evaluation of the expectation value integral in Eq. 4.2.

As mentioned previously, the analyst chooses an array of ground plane points for each scenario evaluated, with sufficient density to give an accurate analysis and covering the projected laser pointing error cone. The grid of ground plane points in MICS coordinates can be described as a set of values, x_j , in the x direction (indexed by j), and y_i , in the y direction (indexed by i). By convention, the neighbouring grid points are defined north, east and northeast of a given grid point. These are found by incrementing j and i ; namely:

$$(x_j, y_i), (x_{j+1}, y_i), (x_j, y_{i+1}) \text{ and } (x_{j+1}, y_{i+1})$$

Note that for a regular grid,

$$x_{j+1} - x_j = x_{j+n} - x_{j+n-1} = \Delta x \quad (4.4)$$

and

$$y_{i+1} - y_i = y_{i+n} - y_{i+n-1} = \Delta y \quad (4.5)$$

where Δx is not necessarily equal to Δy . The ground plane grid points may then be projected onto a unit sphere centered on the aircraft. In this case, the projected ground points will still form a regular pattern in the display axes, in which each quadruplet of ground points $[(x_j, y_i), (x_{j+1}, y_i), (x_j, y_{i+1}), (x_{j+1}, y_{i+1})]$ corresponds to a quadruplet of display axes points in spherical coordinates. The set of all quadruplets of display axes points form the set S of spherical surface areas over which the numerical evaluation (summation) of the integral in Eq. 4.2 is to be performed. To understand how we perform the projection, we must examine the geometric relationship between the ground plane Cartesian coordinate systems, centered on the target, and the display axes coordinate systems, centered on the aircraft.

In Section 3.4 we derived expressions for the colatitude and longitude angles, (θ, ϕ) , using the geometric relationship between the aircraft position, the laser-target vector, the laser projection vector to the ground plane point P , the MICS (x, y, z) axes, and a ground-based display coordinate system with axes (x_D, y_D, z_D) . The z_D -axis was oriented to point directly towards the aircraft, i.e., along the laser-target vector. Now let us define two display axes coordinate systems, centered on the aircraft: a spherical coordinate system (r, θ, ϕ) and a corresponding Cartesian coordinate system (x_s, y_s, z_s) , whose axes are parallel to the axes (x_D, y_D, z_D) . Due to the unique geometric relationship between these two Cartesian coordinate systems, the bearing angles (θ, ϕ) of a ground-based MICS grid point (x, y) can be used to directly define the spherical coordinates (r, θ, ϕ) of an equivalent display axes point, which represents the projection of the ground plane grid point onto a sphere of radius r centered at the aircraft. For a unit sphere, with $r = 1$, the display axes point is essentially defined by the bearing angles (θ, ϕ) calculated from the expressions in Section 3.4.

An illustration of the geometric relationship between the two display axes coordinate systems described above can be seen in Fig. 16. As shown, the spherical coordinates of a point P , on the surface of a sphere of radius r centered at the aircraft, are (r, θ, ϕ) , where r is the radial distance from the origin O (aircraft position), θ is the polar or colatitude angle measured with respect to the (positive) z_s axis, and ϕ is the azimuthal or longitudinal angle from the positive x_s axis. The corresponding Cartesian coordinates, (x_s, y_s, z_s) , of the point P are given by

$$\begin{aligned}
 x_s &= r \sin \theta \cos \phi \\
 y_s &= r \sin \theta \sin \phi \\
 z_s &= r \cos \theta
 \end{aligned}
 \tag{4.6}$$

where $r = 1$ for a unit sphere.

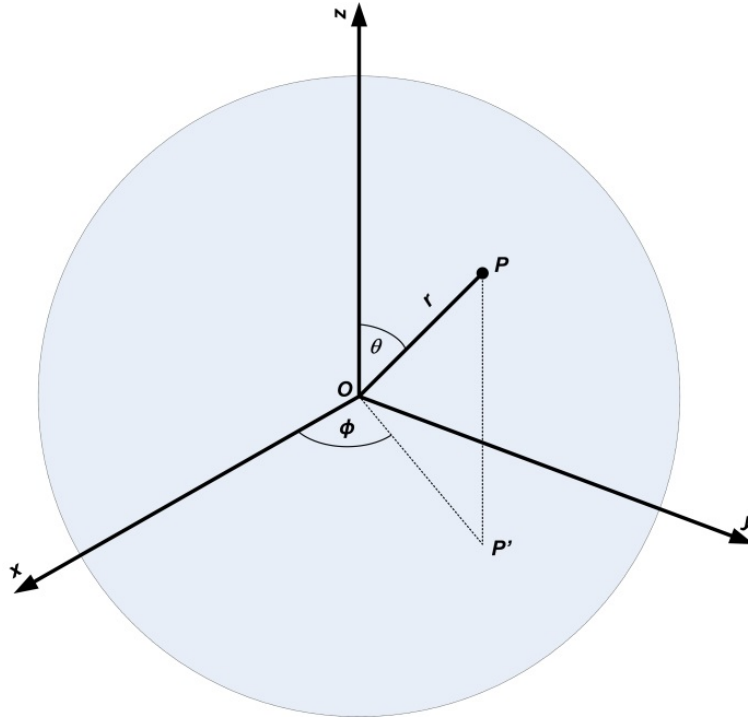


Figure 16: Display Axes Coordinate Systems

It should be noted, from the discussion in Section 3.4, that the positive z_D axis of the ground-based display coordinate system points *upwards* to the aircraft from the target, while the negative z_s axis points downwards to the target from the aircraft. Thus, strictly speaking, the colatitude angle θ should be measured with respect to the *negative* z_s axis. However, in practice, this subtlety will not matter as the aim is simply to determine the spherical area bounded by the array of spherically projected ground points. Once the distribution of spherically projected points has been determined, the orientation of the z_s axis is irrelevant.

The projection of an array of ground points as seen in spherical coordinates is shown in Fig. 17.

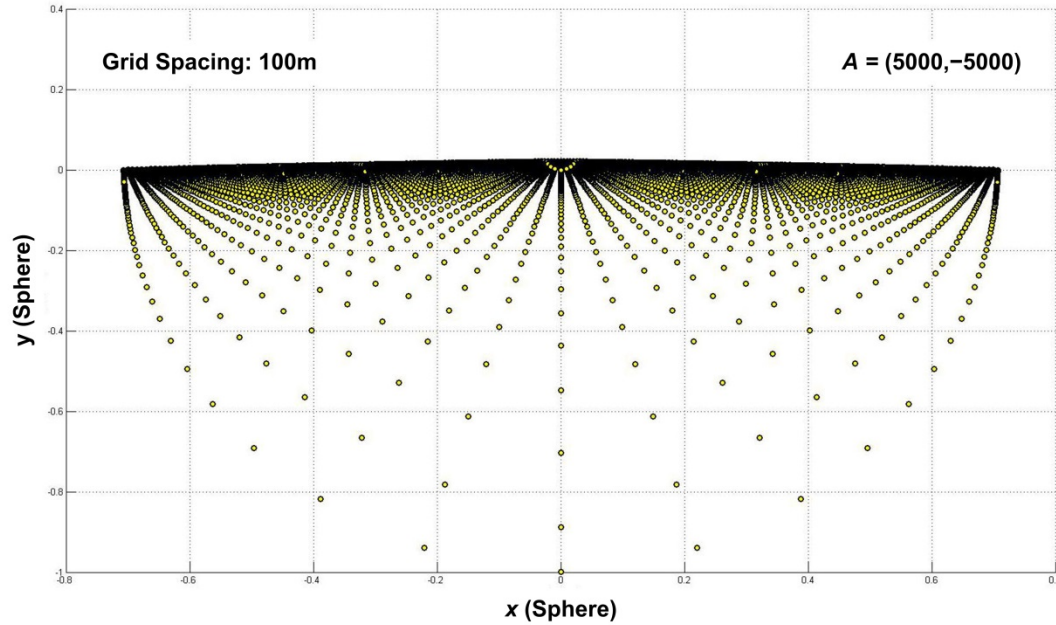


Figure 17: Spherically Projected Array of Ground Points

The spherical area spanned by the array of spherically projected ground points can be approximated by evaluating the area of each quadruplet of points

$$\begin{aligned}
 A &= \left(x_s \left(\theta(x_j, y_i), \phi(x_j, y_i) \right), y_s \left(\theta(x_j, y_i), \phi(x_j, y_i) \right), z_s \left(\theta(x_j, y_i) \right) \right) \\
 B &= \left(x_s \left(\theta(x_{j+1}, y_i), \phi(x_{j+1}, y_i) \right), y_s \left(\theta(x_{j+1}, y_i), \phi(x_{j+1}, y_i) \right), z_s \left(\theta(x_{j+1}, y_i) \right) \right) \\
 C &= \left(x_s \left(\theta(x_{j+1}, y_{i+1}), \phi(x_{j+1}, y_{i+1}) \right), y_s \left(\theta(x_{j+1}, y_{i+1}), \phi(x_{j+1}, y_{i+1}) \right), z_s \left(\theta(x_{j+1}, y_{i+1}) \right) \right) \\
 D &= \left(x_s \left(\theta(x_j, y_{i+1}), \phi(x_j, y_{i+1}) \right), y_s \left(\theta(x_j, y_{i+1}), \phi(x_j, y_{i+1}) \right), z_s \left(\theta(x_j, y_{i+1}) \right) \right)
 \end{aligned}$$

on the surface of the sphere, where $(x_s^{(j)}, y_s^{(i)})$ is the spherically-projected coordinate of the ground point (x_j, y_i) . Each spherical quadruplet can be subdivided into two spherical triangles, namely

$$\begin{aligned}
 A &= \left(x_s \left(\theta(x_j, y_i), \phi(x_j, y_i) \right), y_s \left(\theta(x_j, y_i), \phi(x_j, y_i) \right), z_s \left(\theta(x_j, y_i) \right) \right) \\
 B &= \left(x_s \left(\theta(x_{j+1}, y_i), \phi(x_{j+1}, y_i) \right), y_s \left(\theta(x_{j+1}, y_i), \phi(x_{j+1}, y_i) \right), z_s \left(\theta(x_{j+1}, y_i) \right) \right) \\
 C &= \left(x_s \left(\theta(x_{j+1}, y_{i+1}), \phi(x_{j+1}, y_{i+1}) \right), y_s \left(\theta(x_{j+1}, y_{i+1}), \phi(x_{j+1}, y_{i+1}) \right), z_s \left(\theta(x_{j+1}, y_{i+1}) \right) \right)
 \end{aligned}$$

and

$$A = \left(x_s \left(\theta(x_j, y_i), \phi(x_j, y_i) \right), y_s \left(\theta(x_j, y_i), \phi(x_j, y_i) \right), z_s \left(\theta(x_j, y_i) \right) \right)$$

$$D = \left(x_s \left(\theta(x_j, y_{i+1}), \phi(x_j, y_{i+1}) \right), y_s \left(\theta(x_j, y_{i+1}), \phi(x_j, y_{i+1}) \right), z_s \left(\theta(x_j, y_{i+1}) \right) \right)$$

$$C = \left(x_s \left(\theta(x_{j+1}, y_{i+1}), \phi(x_{j+1}, y_{i+1}) \right), y_s \left(\theta(x_{j+1}, y_{i+1}), \phi(x_{j+1}, y_{i+1}) \right), z_s \left(\theta(x_{j+1}, y_{i+1}) \right) \right)$$

respectively. The geometry of a spherical triangle is illustrated in Fig. 18.

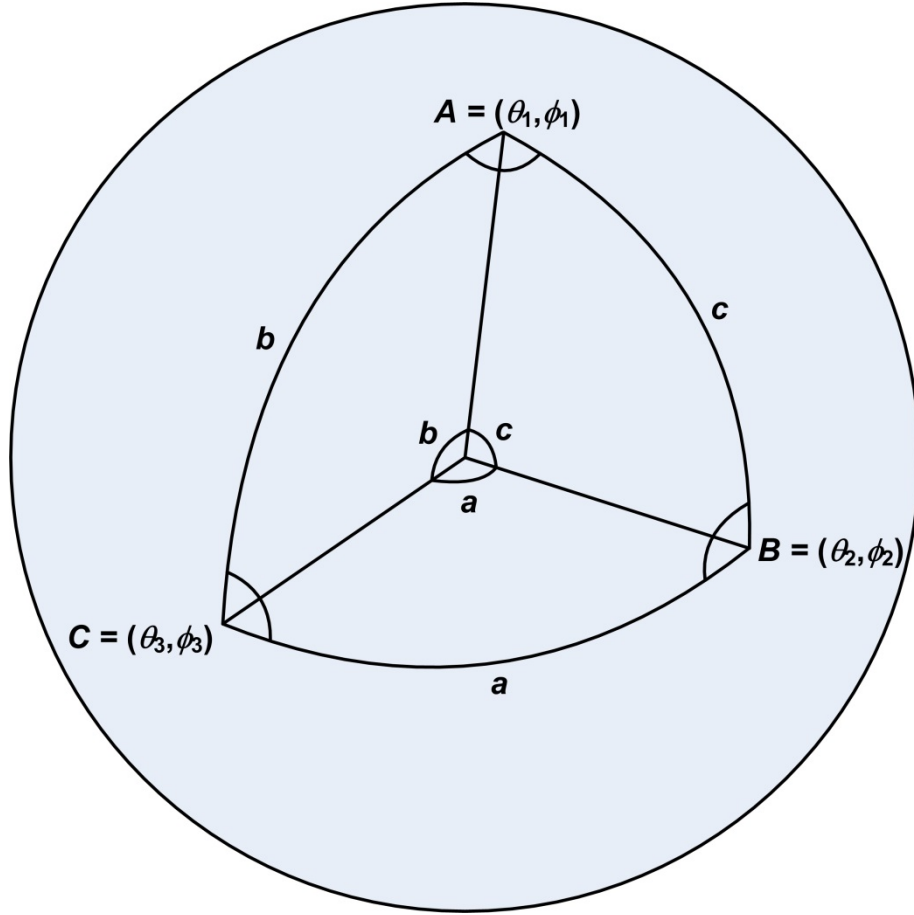


Figure 18: Spherical Triangle

The area ω of the triangle is known as the spherical excess and is given by

$$\omega = a + b + c - \pi \quad (4.7)$$

where a , b , and c are the angles at the vertices A , B , and C of the spherical triangle, respectively. The angles a , b , and c can be evaluated using a combination of the cross and dot products. That is

$$a = \cos^{-1} \left(\frac{(\underline{C} \times \underline{A}) \cdot (\underline{B} \times \underline{A})}{\|\underline{C} \times \underline{A}\| \|\underline{B} \times \underline{A}\|} \right) \quad (4.8)$$

$$b = \cos^{-1} \left(\frac{(\underline{A} \times \underline{B}) \cdot (\underline{C} \times \underline{B})}{\|\underline{A} \times \underline{B}\| \|\underline{C} \times \underline{B}\|} \right) \quad (4.9)$$

and

$$c = \cos^{-1} \left(\frac{(\underline{A} \times \underline{C}) \cdot (\underline{B} \times \underline{C})}{\|\underline{A} \times \underline{C}\| \|\underline{B} \times \underline{C}\|} \right), \quad (4.10)$$

where \underline{A} is the vector OA , \underline{B} is the vector OB and \underline{C} is the vector OC . A similar set of equations can be developed for the angles a , d , and c of the triangle ADC (note the pattern in which the variables occur). Hence, if

$$\omega_{ABC} = a + b + c - \pi \quad (4.11)$$

and

$$\omega_{ADC} = a + d + c - \pi \quad (4.12)$$

are the spherical excesses of the triangles ABC and ADC, then

$$\omega_{ABCD} = \omega_{ABC} + \omega_{ADC} \quad (4.13)$$

is the area of the quadruplet ABCD on the unit sphere. The area of a spherically projected ground plane grid element can hence be evaluated exactly.

4.4 Single Pulse Expectation Value: Numerical Evaluation

We now turn to numerical evaluation methods for the display plane single pulse expectation value given by Eq. 4.2

$$e_{\text{MOVL}} = \iint f(\theta, \phi) g(\theta, \phi) \sin \theta d\theta d\phi$$

Following the same procedure as in the ground plane numerical evaluation discussion of Section 3.7, we will summarize algorithms already presented in Section 4 and clarify the order in which these equations are used in the 3D-CALCFAULT computational flow. Once again the computational flow proceeds from numerical evaluation of the integrand at a single point to numerical evaluation of the integrand over an area. Numerical evaluation of the integral is then achieved by summation of a series of volumes, where each volume represents the product of an elemental spherical area on the unit sphere times the average value of the integrand over that spherical area.

In order to numerically evaluate the integrand at a single point, we must first numerically evaluate each of the two constituent functions of the integrand at that point: the expected number of

observers sustaining a MOVL, $g(\theta, \phi)$, and the display plane laser pointing error PDF, $f(\theta, \phi)$. As in the ground plane evaluation, each of these functions must be numerically evaluated for every set of colatitude and longitude angles (θ, ϕ) , corresponding to the laser pointing errors for every MICS ground plane point (x, y) , which might possibly be struck by the errant laser pulse. Based on the discussion in Section 4.3, the spherical projection of the ground plane point onto the unit sphere produces a display axes point whose spherical coordinates correspond to the bearing angles (θ, ϕ) of the ground plane point.

As in Section 3.7 we begin with calculation of the aircraft bearing angle, the aircraft elevation angle, and the colatitude and longitude angles (θ, ϕ) , representing an aircraft at position $A = (x_A, y_A, z_A)$ in MICS coordinates, firing a laser pulse that strikes the ground plane point $P = (x_P, y_P, z_P)$. This is the calculation presented in Section 3.4, which will not be repeated here. Projection of the ground plane point onto the unit sphere produces a display axes point with spherical coordinates (θ, ϕ) and Cartesian coordinates

$$\begin{aligned} x_s &= \sin \theta \cos \phi \\ y_s &= \sin \theta \sin \phi \\ z_s &= \cos \theta \end{aligned} \tag{4.14}$$

With these preliminary computations complete, we can now numerically evaluate the two constituent functions of the integrand at the ground plane point P . First, the expected number of observers sustaining a MOVL, $g(\theta, \phi)$, is computed from Eq. 3.3

$$g(\theta, \phi) = NQ \left[W_{\text{MOVL}}(h(\theta, \phi)) \right],$$

where the components of $g(\theta, \phi)$ are computed from Eqs. 3.4 - 3.8. As mentioned previously, any form of the display plane laser pointing error PDF, $f(\theta, \phi)$, uniform or non-uniform, can be used for the display plane evaluation. Indeed, this is one of its' greatest advantages. In order to compare the results of the ground and display plane methods, however, we must use the uniform fault laser pointing error distribution given by Eq. 3.31

$$f(\theta, \phi) = \frac{1}{2\pi(1 - \cos \theta_{\max})},$$

where the angular ranges are

$$0 \leq \phi < 2\pi \quad \text{and} \quad 0 \leq \theta \leq \theta_{\max},$$

and θ_{\max} is the maximum fault laser pointing angle. The computations above allow us to numerically evaluate the single pulse expectation value integrand at any specified ground plane point, and at its' corresponding display axes point on the unit sphere.

Proceeding to numerical evaluation of the integrand over an elemental spherical surface area, for each quadruplet of adjacent display axes points on the unit sphere,

$$\begin{aligned} A &= \left(x_s^{(j)}, y_s^{(i)} \right) \\ B &= \left(x_s^{(j+1)}, y_s^{(i)} \right) \\ C &= \left(x_s^{(j+1)}, y_s^{(i+1)} \right) \\ D &= \left(x_s^{(j)}, y_s^{(i+1)} \right) \end{aligned}$$

we can compute the spherical surface area of the quadruplet ABCD, $\omega_{ABCD}^{(j,i)}$, using Eq. 4.13:

$$\omega_{ABCD} = \omega_{ABC} + \omega_{ADC}$$

The spherical excesses of the triangles ABC and ADC are given by Eqs. 4.11 and 4.12

$$\omega_{ABC} = a + b + c - \pi$$

$$\omega_{ADC} = a + d + c - \pi$$

where Eqs. 4.8 to 4.10 give the angles a , b , and c at the vertices A , B , and C of the spherical triangle ABC and a similar set of equations can be developed for the angles a , d , and c at the vertices A , D , and C of the spherical triangle ADC, by substitution of parameters.

Now turning to numerical evaluation of the two constituent functions of the integrand, over the same quadruplet ABCD, we use the same method as in Section 3.7. We take the mean of the values of each constituent function at the four points, and assume that this is the average value over the entire spherical area. Thus we have,

$$\bar{f}^{(j,i)} = \frac{f(\theta^{(j,i)}, \phi^{(j,i)}) + f(\theta^{(j+1,i)}, \phi^{(j+1,i)}) + f(\theta^{(j,i+1)}, \phi^{(j,i+1)}) + f(\theta^{(j+1,i+1)}, \phi^{(j+1,i+1)})}{4} \quad (4.15)$$

and

$$\bar{g}^{(j,i)} = \frac{g(\theta^{(j,i)}, \phi^{(j,i)}) + g(\theta^{(j+1,i)}, \phi^{(j+1,i)}) + g(\theta^{(j,i+1)}, \phi^{(j,i+1)}) + g(\theta^{(j+1,i+1)}, \phi^{(j+1,i+1)})}{4} \quad (4.16)$$

where, for brevity,

$$\begin{aligned}\theta^{(j,i)} &= \theta(x_j, y_i) & \phi^{(j,i)} &= \phi(x_j, y_i) \\ \theta^{(j+1,i)} &= \theta(x_{j+1}, y_i) & \phi^{(j+1,i)} &= \phi(x_{j+1}, y_i) \\ \theta^{(j,i+1)} &= \theta(x_j, y_{i+1}) & \phi^{(j,i+1)} &= \phi(x_j, y_{i+1}) \\ \theta^{(j+1,i+1)} &= \theta(x_{j+1}, y_{i+1}) & \phi^{(j+1,i+1)} &= \phi(x_{j+1}, y_{i+1})\end{aligned}$$

Finally, the contribution to e_{MOVL} from each quadruplet of spherically-projected ground points can be approximated by summation over a series of volumes, where each volume is obtained by multiplying the area ω_{ABCD} by the mean of the integrand values $f(\theta, \phi)g(\theta, \phi)$ at the vertices. Hence, the single pulse expectation value integral of Eq. 4.2 can be approximated by the sum

$$e_{\text{MOVL}} \approx \sum_i \sum_j \bar{f}^{(j,i)} \bar{g}^{(j,i)} \omega_{ABCD}^{(j,i)}, \quad (4.17)$$

where the summation is carried out over all quadruplets of adjacent points on the unit sphere.

4.5 Comparison of Ground Plane and Display Plane Methods

Sections 3.7 and 4.4 summarized the numerical evaluation techniques for the ground plane and display plane evaluations, respectively, of the single pulse expectation value integral. Naturally, we would like to compare the results of the two methods for some test case. As mentioned, however, the algorithms for the ground plane evaluation, given in Section 3, are valid only for the special case of a uniform pointing error distribution. Thus, in comparing the results of the ground and display plane methods, we will use the uniform fault laser pointing error distribution given by Eq. 3.31.

For our test case we will use a Test Range consisting of an MICS ground plane area ± 5 km square, with a user-selectable grid resolution to test algorithm execution times and overall solution accuracy. Grid resolutions of 1000 m square, 100 m square, and 30 m square would correspond to Digital Terrain Elevation Data (DTED) Levels 0, 1, and 2 respectively. An increased grid resolution will result in increased algorithm execution times, but might be expected to increase numerical accuracy and result in better agreement between the results of the two methods. For this specific test case we will use the DTED Level 0 elemental grid area of 1000 m x 1000 m uniformly across the Test Range.

Once again we assume that the Target position is located at MICS (0,0), with the Test Range extending 5 km north and south of the Target, along the MICS y -axis, and 5 km east and west of the Target, along the MICS x -axis. With a 1 km square grid, the Test Range consists of 100 grid elements, each with an elemental area $A = 10^6 \text{ m}^2$. Note that when evaluating constituent functions at single grid points, 121 values will be obtained, since 121 (x, y) grid points (11 x 11) are needed to mark out the 100 (10 x 10) grid areas. A uniform population density of 50 persons km^{-2} has been assumed for the Test Range, except for a circular Controlled Range Area (CRA) of radius 2 km centered on the Target, within which the population density is set to zero.

As indicated in Section 3.4, a fundamental requirement of the single pulse expectation value evaluation is the correct orientation of the aircraft display axes (x_D, y_D, z_D) relative to the aircraft position and the MICS (x, y, z) axes. Section 3.6 indicates that awareness of the MICS quadrant in which the aircraft lies is also fundamental to the evaluation (see Fig. 12). Thus, for a robust test of the methods, we will evaluate the ground plane and display plane values of e_{MOVL} for a single errant laser pulse emitted due to a control system fault/failure at each of eight different aircraft positions, covering the MICS axes and quadrants. Fig. 19 provides an illustration of the aircraft display axes (x_D, y_D, z_D) for aircraft positions aligned with the MICS (x, y, z) axes, namely

- Target North: aircraft at MICS position $(0, 5000)$
- Target West: aircraft at MICS position $(-5000, 0)$
- Target East: aircraft at MICS position $(5000, 0)$
- Target South: aircraft at MICS position $(0, -5000)$.

Fig. 20 provides an illustration of the aircraft display axes for aircraft positions located in the MICS quadrants, namely

- Target North-East: aircraft at MICS position $(5000, 5000)$
- Target South-East: aircraft at MICS position $(5000, -5000)$
- Target North-West: aircraft at MICS position $(-5000, 5000)$
- Target South-West: aircraft at MICS position $(-5000, -5000)$.

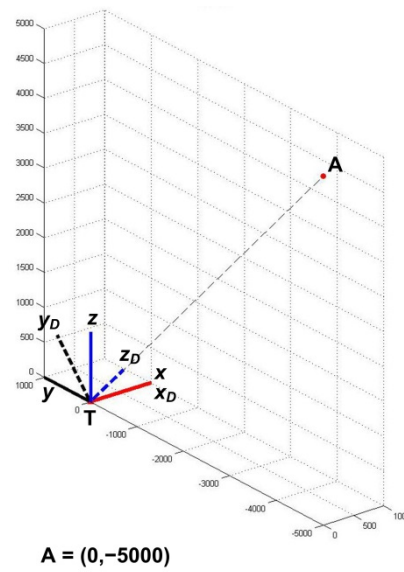
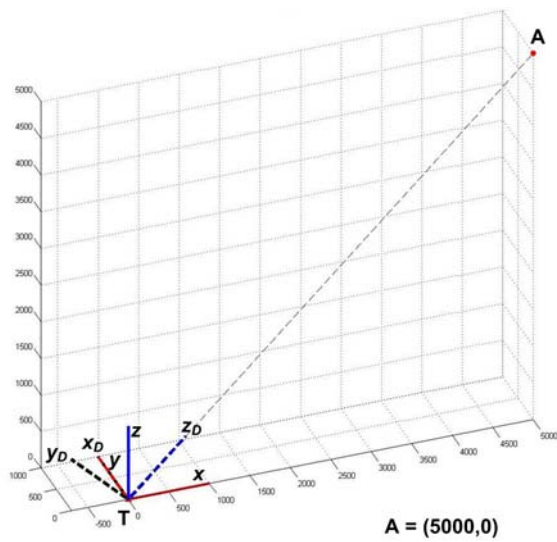
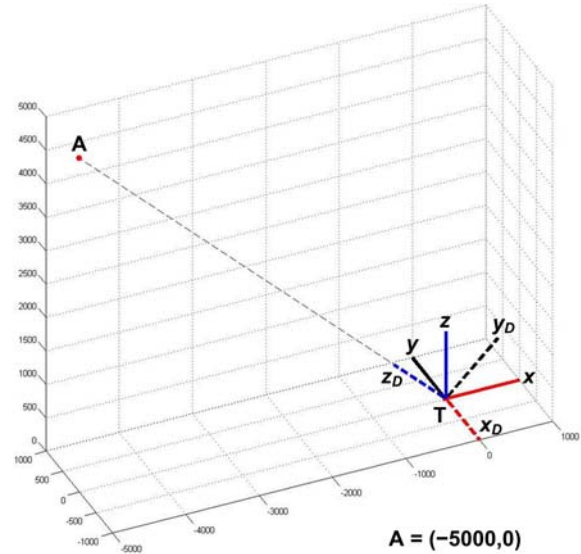
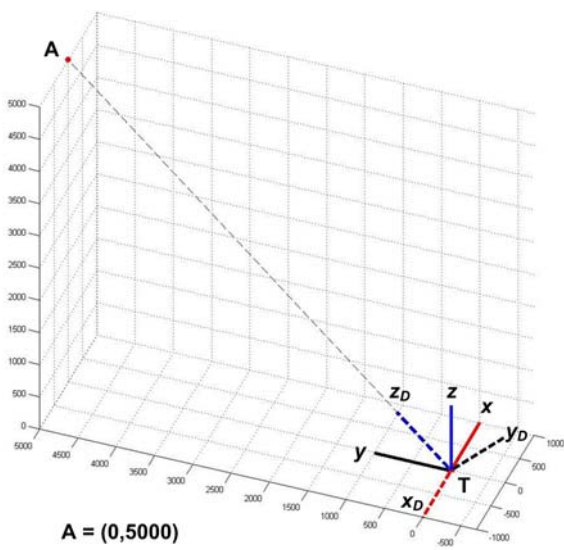


Figure 19: Aircraft Display Axes: Aircraft Aligned with MICS Axes

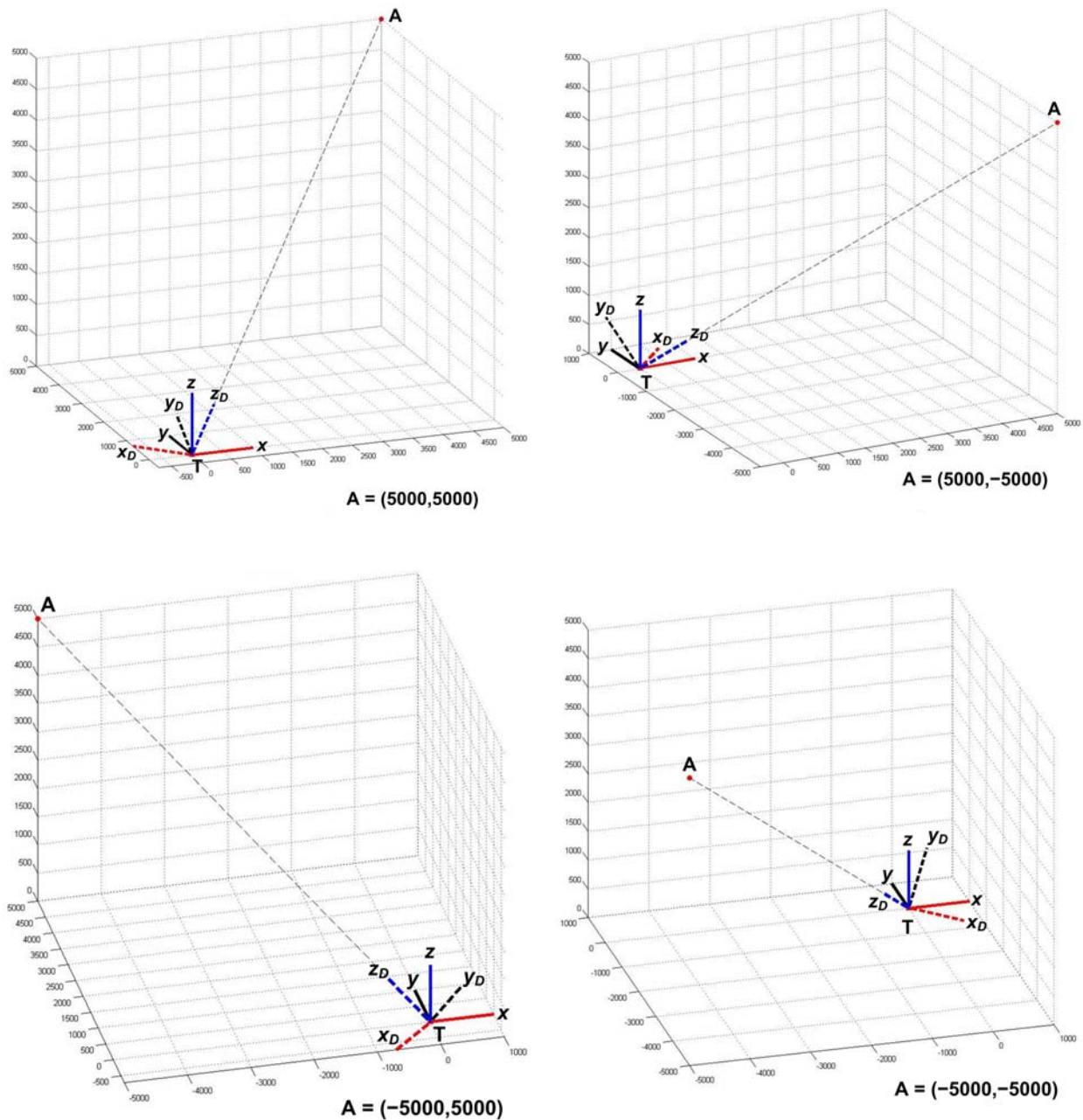


Figure 20: Aircraft Display Axes: Aircraft Located in MICS Quadrants

We should note for clarity that the eight test scenarios illustrated in Figs. 19 and 20 show the aircraft at a variety of heights above the Test Range, mostly quite high (2-5 km), in order to give better angles for visualizing the geometry. For all of our eight test cases, however, the aircraft height will be low and uniform at 1000 feet (304.8 m).

Having laid out the Test Range, grid resolution, CRA, population density on the range, aircraft height, and aircraft positions for our eight test cases, all that remains prior to starting the evalua-

tion is to specify the laser system parameters for the airborne laser designator used to illuminate the Target. For consistency with past work, we will copy the laser system parameters used in a previous test case for MATILDA Version 1.6.1 [16], with a few slight modifications. In that prior test case it was assumed that the airborne laser designator was a multiple pulse “all-round line-of-sight” system mounted on a single-seat strike aircraft. For a complete fault-free and fault laser hazard analysis, important laser input parameters include: i) pulse energy, wavelength, beam divergence, pulse duration, and pulse repetition frequency; ii) Fault-Free and Fault Pointing Error Distributions; and iii) the Probability of Fault and Laser Switch-off Time in Fault Condition for the laser system. These laser system parameters are obtained by the laser system manufacturer, through testing of multiple laser units and averaging of performance data. The data is provided to laser safety officers in the Laser Safety Paper (LSP), mentioned in Section 2.1. The laser system parameters for the airborne laser designator used in our test case are given in Table 1.

Table 1: Laser System Parameters for the Test Case Airborne Laser Designator

Laser System Parameter	Value
Fault-Free Pointing Error Distribution	Gaussian
Fault-Free RMS Pointing Error	5 mrad
Fault Pointing Error Distribution	Uniform
Maximum Fault Pointing Error	0.175 rad (10 deg)
Probability of Fault	10^{-4} per attack
Laser Switch-off Time in Fault Condition	3 seconds
Laser Wavelength	1064 nm
Pulse Energy	200 mJ
Beam Divergence	0.1 mrad
Pulse Duration	10 ns
Pulse Repetition Frequency	20 Hz

Much of the data in Table 1 applies to types of hazard analysis which we will not deal with here. For example, the fault free laser pointing error data would only be used in the fault-free laser hazard analysis, described in Section 2.1. The Probability of Fault, P_F , the Laser Switch-off Time in Fault Condition (3 seconds), and the Pulse Repetition Frequency (20 Hz), would only be

used in evaluating Eq. 3.1, for the overall expectation value, E_{MOVL} , of an unprotected observer sustaining a MOVL as a result of a single fault/failure event. In our current test case analysis, however, we only wish to calculate and compare the fault-condition single pulse expectation values, e_{MOVL} . For this we need the values of the display plane fault laser pointing error PDF, $f(\theta, \phi)$, specified as uniform, and the maximum fault pointing error value of $\theta_{\text{max}} = 10^\circ$. The evaluation of the expected number of observers sustaining a MOVL, $g(\theta, \phi)$, is based on unaided viewing of a laser pulse with the wavelength (1064 nm), pulse duration (10 ns), pulse energy (200 mJ), and beam divergence (0.1 mrad), listed above.

We begin the ground plane evaluation, for the aircraft positions in each of the eight test cases, by calculating the single point values, at each of the 121 grid points, for the colatitude θ , the longitude ϕ , the display plane laser pointing error PDF, $f(\theta, \phi)$, the expected number of observers sustaining a MOVL, $g(\theta, \phi)$, and the Jacobian, $|J(\theta, \phi)|$. Equations 3.17, 3.24, 3.31, 3.3, and 3.55, respectively, are used for these single point calculations. The single point values of the ground-projected laser pointing error PDF, $f_G(\theta, \phi)$, can then be calculated from Eq. 3.10, using the single point values of $f(\theta, \phi)$ and $|J(\theta, \phi)|$.

Next, using the 121 single point values for each of the two constituent parameters of the ground plane integrand, $f_G(\theta, \phi)$ and $g(\theta, \phi)$, we calculate the average values of these constituent parameters, $\bar{f}_G^{(j,i)}$ and $\bar{g}^{(j,i)}$, for each of the 100 elemental grid areas, using Eqs. 3.57 and 3.58, respectively. The elemental area A , from Eq. 3.59, is a constant of value $A = 10^6 \text{ m}^2$. Finally, Eq. 3.56 is used to evaluate the ground plane single pulse expectation value by summing over all grid areas. The single pulse expectation values for each of the eight aircraft positions are:

- Target North: aircraft at MICS position (0,5000); $e_{\text{MOVL}} = 4.2494 \times 10^{-6}$
- Target West: aircraft at MICS position (-5000,0); $e_{\text{MOVL}} = 4.2494 \times 10^{-6}$
- Target East: aircraft at MICS position (5000,0); $e_{\text{MOVL}} = 4.2494 \times 10^{-6}$
- Target South: aircraft at MICS position (0,-5000); $e_{\text{MOVL}} = 4.2494 \times 10^{-6}$
- Target North-East: aircraft at MICS position (5000,5000); $e_{\text{MOVL}} = 2.2036 \times 10^{-4}$
- Target South-East: aircraft at MICS position (5000,-5000); $e_{\text{MOVL}} = 2.2036 \times 10^{-4}$
- Target North-West: aircraft at MICS position (-5000,5000); $e_{\text{MOVL}} = 2.2036 \times 10^{-4}$
- Target South-West: aircraft at MICS position (-5000,-5000); $e_{\text{MOVL}} = 2.2036 \times 10^{-4}$

It should be noted that the symmetries in the e_{MOVL} values match that of the test plane set-up.

We now begin the display plane evaluation, for the aircraft positions in each of the eight test cases, by calculating the single point values, at each of the 121 MICS grid points, for the colatitude θ , the longitude ϕ , the display plane laser pointing error PDF, $f(\theta, \phi)$, and the expected number of observers sustaining a MOVL, $g(\theta, \phi)$. Once again Equations 3.17, 3.24, 3.31, and 3.3,

respectively, are used for these single point calculations. Since the test cases are the same, these values will be identical to those obtained in the ground plane evaluation. For display plane evaluation single point values of the Jacobian, and the corresponding ground-projected laser pointing error PDF, are not needed. We do, however, need the 121 single point values of the (x_s, y_s, z_s) coordinates, corresponding to projection of the ground plane MICS grid points onto a unit sphere centered on the aircraft position. These are calculated from Eq. 4.14.

Next, using the 121 single point values for each of the two constituent parameters of the display plane integrand, $f(\theta, \phi)$ and $g(\theta, \phi)$, we calculate the average values of these constituent parameters, $\bar{f}^{(j,i)}$ and $\bar{g}^{(j,i)}$, for each of the 100 spherical surface areas, using Eqs. 4.15 and 4.16, respectively. The corresponding spherical surface areas on the unit sphere, bounded by all quadruplets of adjacent display axes points ABCD, $\omega_{ABCD}^{(j,i)}$, are calculated using Eq. 4.13 and the procedure laid out in Section 4.4. Finally, Eq. 4.17 is used to evaluate the display plane single pulse expectation value by summing over all spherical areas. The single pulse expectation values for each of the eight aircraft positions are:

- Target North: aircraft at MICS position $(0, 5000)$; $e_{\text{MOVL}} = 3.3495 \times 10^{-6}$
- Target West: aircraft at MICS position $(-5000, 0)$; $e_{\text{MOVL}} = 3.3495 \times 10^{-6}$
- Target East: aircraft at MICS position $(5000, 0)$; $e_{\text{MOVL}} = 3.3495 \times 10^{-6}$
- Target South: aircraft at MICS position $(0, -5000)$; $e_{\text{MOVL}} = 3.3495 \times 10^{-6}$
- Target North-East: aircraft at MICS position $(5000, 5000)$; $e_{\text{MOVL}} = 8.6201 \times 10^{-6}$
- Target South-East: aircraft at MICS position $(5000, -5000)$; $e_{\text{MOVL}} = 8.6201 \times 10^{-6}$
- Target North-West: aircraft at MICS position $(-5000, 5000)$; $e_{\text{MOVL}} = 8.6201 \times 10^{-6}$
- Target South-West: aircraft at MICS position $(-5000, -5000)$; $e_{\text{MOVL}} = 8.6201 \times 10^{-6}$

It should be noted that the symmetries in the e_{MOVL} values match that of the test plane set-up.

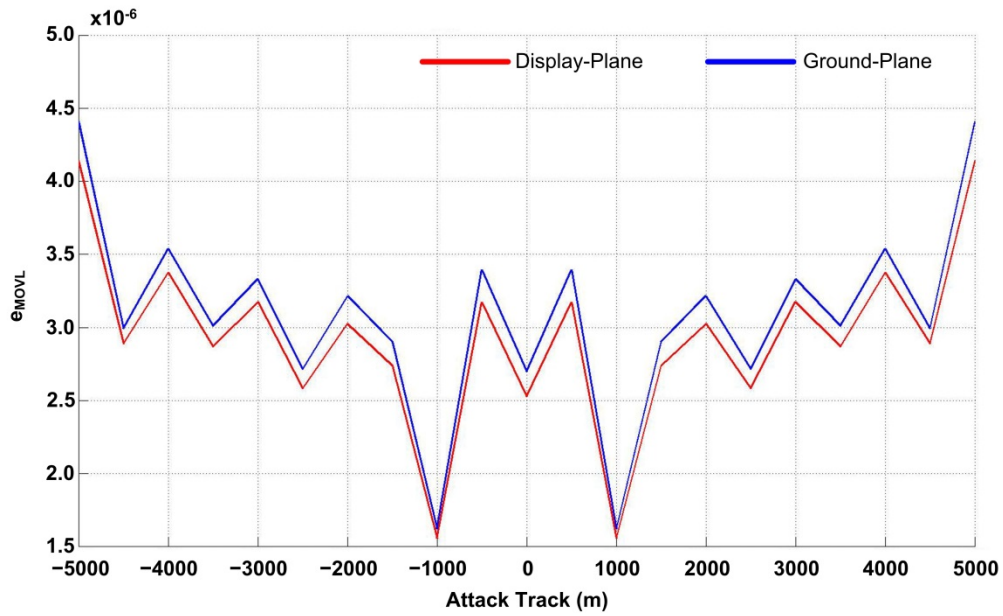
Comparing results, there is clearly a discrepancy between the expectation values calculated using the two different evaluation methods, with the ground plane values being higher than the corresponding display plane values, significantly so for the off-axis aircraft positions in the four quadrants. Given the low grid resolution (1000 m square) in our initial test case, it is logical to assume that a higher grid resolution might produce better convergence in the comparative results. To test this we now compute the variation in e_{MOVL} along a simulated attack track, using both evaluation methods.

For this new test case, the same Test Range, CRA, population density on the range, aircraft height, and laser system parameters were used as in the initial test case above. Four different grid resolutions were used (500 m, 250 m, 100 m, 25 m), to show the effect of differing grid resolutions on the evaluation of e_{MOVL} . The aircraft positions were defined by an attack track consisting of a straight line along one side of the Test Range, such that:

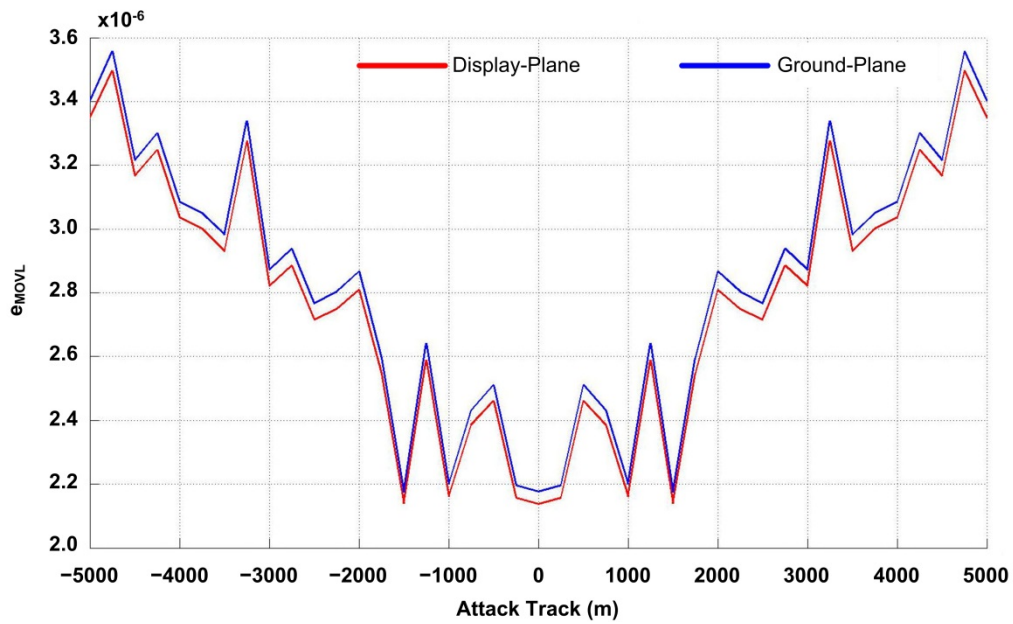
- The aircraft “ x ” coordinate varies between $x = -5000$ and $x = 5000$ in steps of x_{inc}
- The aircraft “ y ” coordinate is held constant at $y = 5000$

Thus, the aircraft tracks along the northern edge of the Test Range from the northwest to the northeast, where the step size, x_{inc} , is assumed to correspond to one of the four grid resolutions listed above. It was also assumed that a single laser pulse is fired from each grid point (or step), producing a single pulse expectation value that can be plotted as a function of aircraft position along the attack track.

The results of these calculations, for the four grid resolutions and two evaluation methods, are plotted in Figures 21 and 22. The results for 500 m and 250 m resolution are shown in Figures 21(a) and 21(b), respectively. The results for 100 m and 25 m resolution are shown in Figures 22(a) and 22(b), respectively. Two things may be noted here. First, the diagrams indicate clearly that increased grid resolution provides for more accurate evaluation of the single pulse expectation value at any point. Second, increased resolution causes the ground plane and display plane results to converge fairly well, although some discrepancy is still present. Some differences in the calculated values are probably to be expected, due to the different methods of evaluation involved. However, the display plane evaluation is a reasonable, if slightly optimistic, approximation to the ground plane values in all cases, with the closeness of the match improving with increasing Test Range resolution.

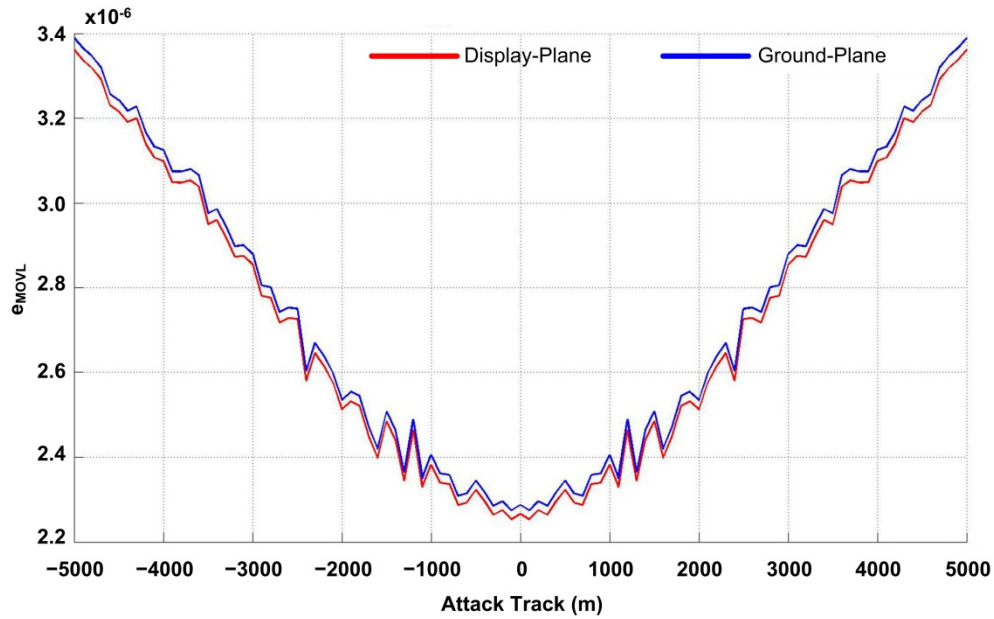


(a) $x_{inc} = 500$ m

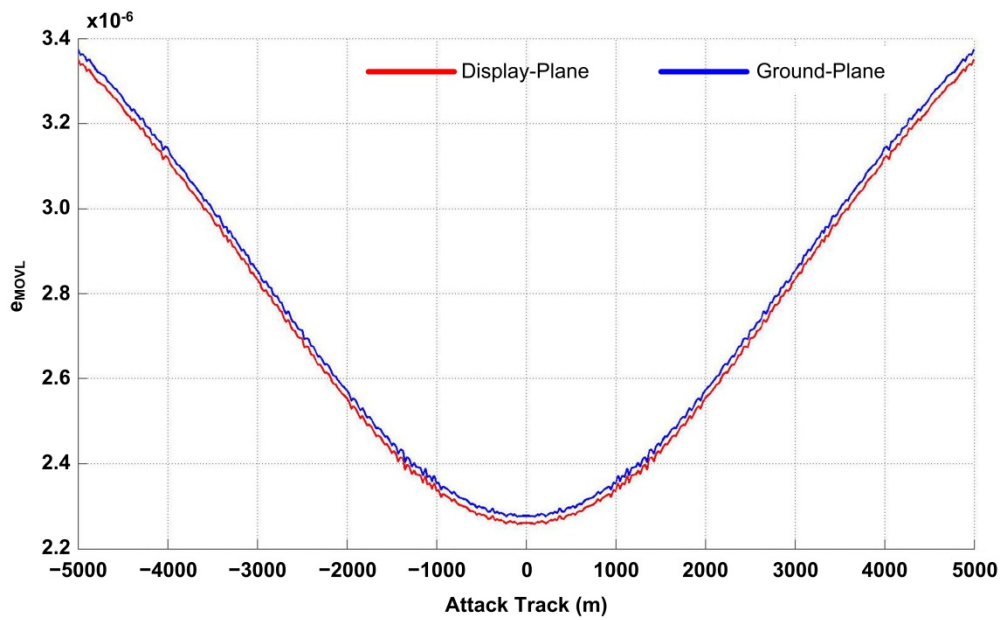


(b) $x_{inc} = 250$ m

Figure 21: Attack Track Expectation Value: 500 m and 250 m Resolution



(a) $x_{inc} = 100$ m



(b) $x_{inc} = 25$ m

Figure 22: Attack Track Expectation Value: 100 m and 25 m Resolution

The attack track results highlight a small, but persistent, difference in the ground plane and display plane evaluations of e_{MOVL} . As a final topic before concluding, we consider the possible factors underlying this discrepancy. The numerical evaluation of the single pulse expectation value involves the summation of a number of non-overlapping elements, each of which is the product of the probability of a laser pointing error (f_G or f) and the expected number of observers sustaining ocular damage (g) occurring within a small elemental area, either on the ground plane or on the surface of the unit sphere. In both the display plane and ground plane methods, the elemental area is defined by the applicable map-based grid spacing.

Comparing Eqs. 3.56 and 4.17, and expressing the ground projected laser pointing error, f_G , in terms of the display plane laser pointing error, f , and the Jacobian

$$f_G = f |J| \quad (4.18)$$

we see that the difference between the two methods is basically the difference between the evaluations of $\omega_{ABCD}^{(j,i)}$ and $|\overline{J}|^{(j,i)} A^{(j,i)}$ in the display plane and ground plane approaches, respectively.

The values of $\omega_{ABCD}^{(j,i)}$ and $A^{(j,i)}$ are exact, whereas the mean $|\overline{J}|^{(j,i)}$ of the Jacobian is only an estimate of its value over the elemental ground plane area, something that potentially introduces additional averaging error into the ground plane evaluation. Logically, any discrepancy introduced by averaging errors in the Jacobian will tend to shrink with increasing grid resolution, since the quadruplet of values averaged will be closer together.

Another factor to consider is that the Jacobian $|J|$ is strictly a modifier of the display plane laser pointing error PDF, while the spherical excess $\omega_{ABCD}^{(j,i)}$ is dependent on r^2 , where r is the radius of the sphere on which the ground plane grid points have been projected. The relationship between $\omega_{ABCD}^{(j,i)}$ and $|\overline{J}|^{(j,i)} A^{(j,i)}$ is hence one of proportionality. In the current analysis, a good approximation has been achieved with a value of $r=1$. We note that increasing aircraft height above the range will also reduce discrepancies in these area dependent quantities, since any ground plane grid area will then project to a smaller solid angle on the unit sphere.

To summarize, the difference in the single pulse expectation value produced by the ground plane and display plane evaluation methods is a function of both grid resolution and aircraft height. It is not likely to be significant except in extreme cases that combine low aircraft height and low grid resolution. Referring back to our original test case, the low aircraft height (304.8 m) and low grid resolution (1000 m) doubtless contributed to the discrepancies seen. This was a deliberate choice, since it allowed a clearer demonstration of the convergence of the two methods for high grid resolution [21].

5 CONCLUSIONS

Over the past 15 years, the United Kingdom (UK) Ministry of Defence (MoD) and the United States (US) Air Force Research Laboratory (AFRL) have collaborated to develop a US-UK laser

range safety tool, the Military Advanced Technology Integrated Laser hazard Assessment (MATILDA) tool. MATILDA uses Probabilistic Risk Assessment (PRA) techniques to perform laser safety and hazard analysis in support of airborne laser designator use during test and training exercises on military ranges. The initial MATILDA tool, MATILDA PRO Version-1.6.1, was based on the 2007 PRA model developed to perform range safety clearances for the UK Thermal Imaging Airborne Laser Designator (TIALD) system. The 2007 TIALD model was an approximation that assumed flat terrain on the range (Smooth Earth TIALD Model), a conservative approximation valid in all terrain. Over the past five years, however, an enhanced version, MATILDA PRO Version-2.0.3, has been produced. The enhanced tool is based on an updated (2012) TIALD model, which has more complex PRA algorithms appropriate for hilly terrain (Rough Earth TIALD Model).

The Rough Earth TIALD Model has four major computational modules: 3D-RBPROG, 3D-CALCZONE, 3D-CALCTERT, and 3D-CALCFAULT. The first deals with creation of a three-dimensional Controlled Range Area (3D-CRA). The second and third perform the laser hazard analysis for fault-free laser operation. The primary product of the fault-free laser hazard analysis is the Fault-Free Laser Firing Zones (FFLFZ), a geometric area within which an aircraft flying at a designated altitude can fire freely at the target. The fourth module, 3D-CALCFAULT, performs a probabilistic hazard analysis for laser operation in the fault/failure condition; i.e., when the laser directional control system breaks lock on the target and allows one or more laser pulses to escape the CRA. The product of the probabilistic fault/failure laser hazard analysis is the expectation value: the likelihood that an unprotected observer outside the CRA will suffer ocular injury as a result of the directional control failure.

For reasons of length, documentation of the mathematical algorithms and computational procedures incorporated in MATILDA PRO Version-2.0.3 has been divided between two AFRL Technical Reports, which will provide the mathematical basis for future code development. This Technical Report, designated Part I, contains documentation of the computational procedures for two different methods of probabilistic fault/failure laser hazard analysis. Section 3 documents the revisions which have been made, since 2012, in the old CALCFAULT module, which performs the probabilistic fault/failure hazard evaluation in the Ground Plane of the target, using Cartesian Coordinates. The revisions relate to the form and derivation of the Jacobian function used to transform the fault laser pointing error Probability Distribution Function (PDF), $f(\theta, \phi)$, in the aircraft display plane, to the PDF of the ground-projected fault laser pointing errors, used in the ground plane evaluation.

The changes in the original CALCFAULT algorithms were necessary to provide continuity with algorithms for the new 3D-CALCFAULT module, documented in Section 4. 3D-CALCFAULT performs the probabilistic fault/failure hazard evaluation in the Display Plane of the aircraft, using Spherical Coordinates. The shift to probabilistic hazard evaluation in the display plane produces simplification of the algorithms, with increased efficiency and speed of computation, since no Jacobian transformation is needed for display plane evaluation of the single pulse expectation value. Another advantage is that any form of the display plane fault laser pointing error PDF, uniform or non-uniform, can be used for display plane evaluation. Ground plane evaluation can only be done for a uniform display plane fault laser pointing error distribution, which is the special case for which the ground plane algorithms are valid. Finally, display plane evaluation is better suited for probabilistic laser hazard evaluation in hilly terrain.

Comparison of the results of the two probabilistic fault/failure hazard evaluation methods, performed for several test cases using a uniform fault laser pointing error PDF, indicates that the single pulse expectation values computed tend to match fairly well, with the closeness of the match improving with higher Test Range grid resolution and greater aircraft height above the range. The difference is not likely to be significant, except in extreme cases that combine low aircraft height and low grid resolution. The second Technical Report, designated Part II, will document the mathematical algorithms and computational procedures for fault-free laser hazard analysis using the Rough Earth TIALD Model, and will cover the remaining computational modules: 3D-RBPROG, 3D-CALCZONE, and 3D-CALCTERT.

6 REFERENCES

1. *MIL-HDBK-828A: Laser Safety on Ranges and in Other Outdoor Areas*, DOD Handbook, Department of Defense, Washington, DC (1996).
2. *JSP 390, Military Laser Safety: Volume 2 – Laser Safety Management System (2012 Edition)*, UK Ministry of Defence, London, UK (2012).
3. American National Standards Institute, *ANSI Standard Z136.1-2014: American National Standard for Safe Use of Lasers*, Laser Institute of America, Orlando, Florida (2014).
4. International Electrotechnical Commission, *IEC 60825-1-2015: Safety of Laser Products, Part 1 – Equipment Classification and Requirements*, Geneva, Switzerland (2015).
5. Bedford, T. and Cooke, R. M., *Probabilistic Risk Analysis: Foundations and Methods*, Cambridge University Press, Cambridge, UK (2001).
6. Kumamoto, H. and Henley, E. J., *Probabilistic Risk Assessment and Management for Engineers and Scientists (Second Ed.)*, Institute of Electrical and Electronic Engineers, Inc., New York, NY (1996).
7. Smith, P. A., *J. Laser Appl.* **6**, 101 (1994).
8. Sliney, D. H., *Optics and Laser Tech.* **27**, 279 (1995).
9. Gardner, R. and Smith, P. A., *Optics and Laser Tech.* **27**, 15 (1995).
10. Smith, P. A., Van Veldhuizen, D. A. and Polhamus, G. D., “High-Energy Laser Systems: Analytical Risk Assessment and Probability Density Functions,” *Proceedings of the SPIE* **4246**, 145 (2001).
11. Flemming, B. K., “A Probabilistic Risk Assessment Process for High-Power Lasers on Outdoor Ranges,” *Proceedings of the International Laser Safety Conference* **12**, 171 (2015).
12. Flemming, B. K., Kennedy, P. K., Huantes, D. F., and Flower, M. D., “Probabilistic Risk Assessment Process for High-Power Laser Operations in Outdoor Environments,” *DEPS Journal of Directed Energy* **5**, 381 (2016).

13. Flemming, B. K., Huantes, D. F. and Kennedy, P. K., "MATILDA: A Laser Range Hazard Assessment Utility," *Proceedings of the International Laser Safety Conference* **10**, 239 (2011).
14. Flemming, B. K., Grieve, L. M., Huantes, D. F., Kennedy, P. K. and Flower, M. D., "Laser System Safety Investigations for PRA Model Development," *Proceedings of the International Laser Safety Conference* **11**, 118 (2013).
15. Flemming, B. K., Kennedy, P. K., Huantes, D. F., and Flower, M. D., "MATILDA: A Military Laser Range Safety Tool Based on Probabilistic Risk Assessment Techniques," *DEPS Journal of Directed Energy* **5**, 237 (2014).
16. Kennedy, P. K., Flemming, B. K., Huantes, D. F., and Flower, M. D., "MATILDA: A Military Laser Range Safety Tool Based on Probabilistic Risk Assessment (PRA) Techniques," DOD Technical Report No. AFRL-RH-FS-TR-2014-0035, U. S. Air Force Research Laboratory, Fort Sam Houston, TX (2014).
17. Huantes, D. F., Kennedy, P. K., Flemming, B. K., and Flower, M. D., "PRA Analysis of Attack Track Suitability," *Proceedings of the International Laser Safety Conference* **12**, 126 (2015).
18. *Health and Safety at Work Act 1974 (c. 37)*, Her Majesty's Stationary Office, London, UK (1974).
19. Covello, V.T. and Merkhofer, M.W., *Risk Assessment Methods: Approaches for Assessing Health and Environmental Risks*, Plenum Press, New York, NY (1993).
20. Flemming, B. K., and Harding, S. J., *PRA MoU: CALCFAULT Algorithm Ground-Plane Evaluation*, Leonardo Airborne & Space Systems Technical Report: AP50043054, Revision 4, Leonardo MW Ltd., Edinburgh, UK (2016).
21. Flemming, B. K., and Harding, S. J., *Development of the CALCFAULT Algorithm for Hilly Terrain*, Leonardo Airborne & Space Systems Technical Report: AP50072768, Revision 4, Leonardo MW Ltd., Edinburgh, UK (2016).